

The First Hour of Extra-galactic Data of the Sloan Digital Sky Survey Spectroscopic Commissioning: The Coma Cluster.

Francisco J. Castander^{1,2}, Robert C. Nichol³, Aronne Merrelli^{3,4}, Scott Burles^{1,6}, Adrian Pope^{3,5}, Andrew J. Connolly⁹, Alan Uomoto⁵, James E. Gunn¹⁰, John E. Anderson⁶, James Annis⁶, Neta A. Bahcall¹⁰, William N. Boroski⁶, Jon Brinkmann⁷, Larry Carey⁸, James H. Crocker⁵, István Csabai^{5,18}, Mamoru Doi¹³, Joshua A. Frieman^{6,1}, Masataka Fukugita^{14,15}, Scott D. Friedman⁵, Eric J. Hilton³, Robert B. Hindsley¹⁶, Željko Ivezić¹⁰, Steve Kent⁶, Donald Q. Lamb¹, R. French Leger⁸, Daniel C. Long⁷, Jon Loveday²⁰, Robert H. Lupton¹⁰, Harvey MacGillivray¹¹, Avery Meiksin¹¹, Jeffrey A. Munn¹⁷, Matt Newcomb³, Sadanori Okamura¹³, Russell Owen⁸, Jeffrey R. Pier¹⁷, Constance M. Rockosi¹, David J. Schlegel¹⁰, Donald P. Schneider¹², Walter Seigmund⁸, Stephen Smee⁵, Yehuda Snir³, Larry Starkman⁸, Chris Stoughton⁶, Gyula P. Szokoly¹⁹, Christopher Stubbs⁸, Mark SubbaRao¹, Alex Szalay⁵, Christy Tremonti⁵, Patrick Waddell⁸, Brian Yanny⁶ and Donald G. York¹

ABSTRACT

On 26 May 1999, one of the Sloan Digital Sky Survey (SDSS) fiber-fed spectrographs saw astronomical first light. This was followed by the first spectroscopic commissioning run during the dark period of June 1999. We present here the first hour of extra-galactic spectroscopy taken during these early commissioning stages: an observation of the Coma cluster of galaxies. Our data samples the Southern part of this cluster, out to a radius of 1.5 degrees ($1.8 h^{-1}$ Mpc, approximately to the virial radius) and thus fully covers the NGC 4839 group. We outline in this paper the main characteristics of the SDSS spectroscopic systems

¹The University of Chicago, Astronomy & Astrophysics Center, 5640 S. Ellis Ave., Chicago, IL 60637

²Observatoire Midi-Pyrénées, 14 ave Edouard Belin, Toulouse, F-31400, France

³Department of Physics, Carnegie Mellon University, 5000 Forbes Ave., Pittsburgh, PA-15232

⁴Department of Astronomy, California Institute of Technology, Pasadena, CA 91125

⁵ Department of Physics & Astronomy, The Johns Hopkins University, 3701 San Martin Drive, Baltimore, MD 21218, USA

⁶Fermi National Accelerator Laboratory, P.O. Box 500, Batavia, IL 60510

⁷Apache Point Observatory, P.O. Box 59, Sunspot, NM 88349-0059

⁸University of Washington, Department of Astronomy, Box 351580, Seattle, WA 98195

⁹Department of Physics & Astronomy, University of Pittsburgh, Pittsburgh, PA 15260

¹⁰Princeton University Observatory, Princeton, NJ 08544

¹¹Royal Observatory, Edinburgh, EH9 3HJ, United Kingdom

¹²Department of Astronomy & Astrophysics, Pennsylvania State University, University Park, PA 16802

¹³Department of Astronomy & Research Center for the Early Universe, School of Science, University of Tokyo, Hongo, Bunkyo, Tokyo, 113-0033, Japan

¹⁴Institute for Cosmic Ray Research, University of Tokyo, Midori, Tanashi, Tokyo 188-8502, Japan

¹⁵Institute for Advanced Study, Olden Lane, Princeton, NJ 08540

¹⁶Remote Sensing Division, Naval Research Laboratory, 4555 Overlook Ave. SW, Washington, DC 20375

¹⁷U.S. Naval Observatory, Flagstaff Station, P.O. Box 1149, Flagstaff, AZ 86002-1149

¹⁸Department of Physics of Complex Systems, Eötvös University, Pázmány Péter sétány 1/A, Budapest, H-1117, Hungary

¹⁹Astrophysikalisches Institut Potsdam, An der Sternwarte 16, D-14482 Potsdam, Germany

²⁰Astronomy Center, University of Sussex, Falmer, Brighton BN1 9QJ, UK

and provide redshifts and spectral classifications for 196 Coma galaxies, of which 45 redshifts are new. For the 151 galaxies in common with the literature, we find excellent agreement between our redshift determinations and the published values, *e.g.*, for the largest homogeneous sample of galaxies in common (63 galaxies observed by Colless & Dunn 1996) we find a mean offset of 3 km s^{-1} and an RMS scatter of only 24 km s^{-1} . As part of our analysis, we have investigated four different spectral classification algorithms: measurements of the spectral line strengths, a principal component decomposition, a wavelet analysis and the fitting of spectral synthesis models to the data. We find that these classification schemes are in broad agreement and can provide physical insight into the evolutionary histories of our cluster galaxies. We find that a significant fraction (25%) of our observed Coma galaxies show signs of recent star-formation activity and that the velocity dispersion of these active galaxies (emission-line and post-starburst galaxies) is 30% larger than the absorption-line galaxies. We also find no active galaxies within the central (projected) $200 h^{-1} \text{ Kpc}$ of the cluster. The spatial distribution of our Coma active galaxies is consistent with that found at higher redshift for the CNOC1 cluster survey. Beyond the core region, the fraction of bright active galaxies appears to rise slowly out to the virial radius and are randomly distributed within the cluster with no apparent correlation with the potential merger or post-merger of the NGC 4839 group. We briefly discuss possible origins of this recent galaxy star-formation.

Subject headings: cosmology: observations – galaxies: clusters: individual (Coma) – galaxies: fundamental parameters – methods: data analysis – catalogs

1. Introduction

The Coma cluster is the richest cluster of galaxies in our local universe and has thus attracted considerable attention over the last century (see reviews by Biviano 1998 & West 1998). In the optical, for example, Goldwin, Metcalfe & Peach (1983; hereafter GMP83) have published an extensive photometric study of the cluster providing accurate positions, colors, magnitudes and ellipticities for 6724 bright galaxies over 2.63 square degrees centered on Coma. Several authors have explored the fainter dwarf galaxy population of Coma (see Bernstein et al. 1995; Kashikawa et al. 1998; Adami et al. 1998 & 2000). The dynamics of the cluster have also been well studied. Kent & Gunn (1982) assembled approximately 300 optical redshifts from the literature to determine the cluster mass distribution. This initial work was extended by Colless & Dunn (1996; CD96), who collected 556 redshifts

(based on new and literature redshifts), and Geller, Diaferio & Kurtz (1999) who have extended the dynamical study of Coma to large radii (10 degrees) and larger numbers (1693 redshifts) thus measuring the density profile of Coma well beyond the virial radius of the cluster. Hughes (1989) measured the total mass of Coma using early X-ray observations of the cluster. More recently, ROSAT observations of Coma have provided unprecedented detail of the intracluster gas morphology (e.g., Briel, Henry & Böhringer 1992; White, Briel & Henry 1993). ASCA observations of the cluster have provided important information on the temperature structure of the X-ray emitting gas (Honda et al. 1996).

The Coma cluster has long been regarded as the archetypal relaxed massive cluster of galaxies. However, recent studies of the cluster have shown otherwise. The current view of Coma is that the cluster is the product of one recent, and one ongoing, cluster-group merger. A group centered on NGC 4839, in the southwest region of the cluster, is falling into (CD96), or has just passed through (Burns et al 1994), the main body of the cluster. The velocity dispersion of this southwest group is approximately $\frac{1}{3}$ of that of the main cluster. Meanwhile, the core of Coma has two dominant galaxies, NGC 4874 and NGC 4889, which seem to be the relic central galaxies of previous groups that have merged into the current cluster. The X-ray and dynamical data reveal that both of these dominant galaxies do not appear to sit at the bottom of the cluster potential (CD96; White, Briel & Henry 1993). The lack of a cooling flow and the existence of an extended radio halo support this merging history of the cluster.

The Coma cluster was thus an ideal first target for the Sloan Digital Sky Survey (SDSS; York et al 2000) spectroscopic commissioning program because of its location (the North Galactic Pole), the pre-existence of wide-field galaxy photometry (e.g. GMP83), and the high-density of known redshifts for comparison and testing. Moreover, there remain interesting scientific questions that can be addressed using the unique SDSS spectroscopic hardware. In this paper, we present the first hour of extra-galactic data taken by the SDSS spectroscopic system. This has produced nearly 200 Coma redshifts thus illustrating the capabilities of this new instrumentation. In §2, we briefly highlight the main characteristics of the SDSS spectroscopic system. In §3, we describe the selection of galaxy targets in the Coma cluster region. The observations of the Coma cluster plates are presented in §4. In §5, we describe the data analysis. We discuss the redshift measurements in §6 and classify the galaxy members in §7. Finally, we discuss our data and present our conclusions in §8.

2. The SDSS Spectroscopic System

The SDSS will use a dedicated 2.5m telescope with a 3 degree field-of-view and two fiber-fed double spectrographs to measure the redshifts of approximately a million galaxies and one hundred thousand quasars over the next 5 years. The SDSS will also image the same area of the sky to an approximate depth of ~ 23 mag in five optical bands (u' , g' , r' , i' and z' ; Fukugita et al 1996; Fan et al 2000). For more details on the SDSS, the reader is referred to York et al 2000 for a brief overview of the survey hardware, software and strategy²¹. The full details of the SDSS spectroscopic system will be presented in Uomoto et al. (2001; in preparation) and Frieman et al. (2001; in preparation). For completeness, we provide here an outline of the SDSS spectroscopic system.

The SDSS spectrographs are designed to cover the wavelength range of $3900 \rightarrow 9100 \text{ \AA}$. This is achieved using a dichroic beamsplitter centered at $\simeq 6000 \text{ \AA}$ to separate the incoming light onto a red and blue camera in both spectrographs. The SDSS spectrographs achieve a spectral resolution of 1800 across its entire spectral range. Each spectrograph accepts 320 fibers, each of which subtends a diameter of $3''$ on the sky. The fibers are plugged into aluminum plug-plates sitting in the focal plane of the SDSS telescope. Each plate contains 640 science holes (one for each science fiber), light-trap holes (drilled to avoid the reflection of light from bright stars off the plug-plate back into the telescope optics), guide star holes (11 in total which are fed to the guide camera) and quality assurance holes.

During normal operations, plates scheduled for observation are manually plugged during the day. Each plug-plate is mounted in an individual cartridge that possesses a full set of 640 science fibers and 11 coherent fiber bundles that are plugged into the guide star holes and used to guide the telescope. Once plugged, the cartridges are automatically mapped with a video system that measures the plug-plate location of each fiber (*i.e.* sky coordinates) as they are successively illuminated by a laser diode at the slithead. After mapping the cartridges are stored ready for mounting on the SDSS telescope during the night.

3. Target Selection

In normal survey operations, the SDSS will select targets for spectroscopic observation using the SDSS photometric survey. However, in the case of the Coma cluster, the SDSS imaging photometric camera had not yet observed this region of the sky and thus target

²¹In addition, the reader can refer to the online SDSS Project Book at <http://www.astro.princeton.edu/PBOOK/welcome.html>

selection was performed using an external catalog.

We have used the SuperCOSMOS scans of two photographic plates (J and O), centered on the Coma cluster (see <http://www-wfau.roe.ac.uk/sss/> for details) kindly provided to us by Harvey MacGillivray. The passband of the J plate is the combination of the Kodak IIIaJ emulsion and a GG395 filter (same as the UK Schmidt b_j system; see Nichol, Collins & Lumsden 2000), while the passband of the O plate is the combination of the IIIaF emulsion and a OG590 filter. The raw object lists of these two SuperCOSMOS scans contain approximately 150,000 objects per plate and therefore must be trimmed for our purposes.

We first merged the two photographic plates catalogs keeping only objects that matched to within 1.5 arcseconds. This merged catalog was separated into a list of stars and galaxies using the SuperCOSMOS source classifier. We produced two lists; one of stellar sources, which were objects classified as stars on both plates, and one of galaxies, which were objects classified as galaxies on at least one of the plates. We used these criteria since star-galaxy separation becomes increasingly difficult at the fainter magnitudes. By including sources which were classified as a galaxy in one plate, but as a star in the other, we hoped to recover some of the faint galaxy population that would have otherwise been missed. Unfortunately, we can expect higher stellar contamination (especially from blended stars) in our galaxy list.

We photometrically calibrated the SuperCOSMOS data using the GMP83 catalog. We matched our galaxy list to the GMP83 data and then derived a transformation to convert the SuperCOSMOS instrumental magnitudes into the GMP83 magnitude system which was calibrated using B -band photoelectric magnitudes for their blue band and $B - R$ colors for their red band (see GMP83 for details). Our photometry is thus measured in the blue and red "photographic bands" (emulsion + filter described above) but transformed to the GMP83 system with a zero-point and color terms. Hereafter, we will refer to these magnitudes as, b and r , following the notation in GMP83. Finally, a small astrometric correction was applied by correlating our star catalog with the ACT star reference catalog.²²

The resulting list of galaxies contained nearly 33,000 objects. This was further trimmed to 8187 targets by imposing a magnitude cut of $14 \leq b \leq 20$. From these targets, a total of 10 plates were designed, with two plates at each of the five plate centers shown in Figure 1. Each pair of plates was allocated unique targets, with one plate containing the brighter galaxies and the other containing the fainter galaxies (see figure 2). This was done for two reasons; first, to accommodate the minimum spacing restriction between SDSS fibers (55 arcseconds) and second, to allow for different exposure times for these plates. Finally, each

²²The ACT catalog is produced by the US Naval Observatory, see <http://aries.usno.navy.mil/ad/act/act.html>

plate was allocated a set of 10 bright stars ($14 < b < 15$) for the guide camera fibers. Since these were selected from the same SuperCOSMOS data there was little concern about their relative astrometric reference frame.

4. Observations

One of the SDSS spectrographs saw first astronomical light on 26 May 1999 in bright time. After this milestone, the first spectroscopic commissioning run took place in the dark period of June 1999. At the time of the Coma SDSS spectroscopic observations, several parts of the nominal SDSS spectroscopic system were either not available or were being commissioned for the first time. For example, only one of the two SDSS spectrographs was mounted on the back of the telescope. Therefore, only 320 science fibers were available per plate instead of the 640 which is now the standard number. In addition, the plate-mapper, which automatically matches the plugged fibers to the target catalog, was not fully automated and we were forced to map the plate by hand. The telescope was not properly collimated at the time of the observations and the hardware needed to obtain spectroscopic calibrations was not installed. Finally, condensation on the front of the red camera dewar produced a series of bright “doughnuts” in the center of the red CCD images rendering most of the red spectrograph data in this commissioning run almost impossible to use.

On 6 June, the SDSS observed plate 133 (the bright plate at the center of Coma). We took two 900 second exposures at mean airmasses of 1.53 and 1.66 without guiding. On 8 June, plate 133 was re-observed taking three 1200 second exposures. These were the first astronomical exposures in which the SDSS spectroscopic system guided on the sky. The seeing was between 1.2 and 1.5 arcseconds and the mean airmasses were 1.07, 1.10 and 1.15 for the three exposures. Being near the zenith, the atmospheric differential refraction effects were small. In addition to plate 133, we also observed plates 135 and 136 on 8 June 1999, which were designed using SDSS photometry in areas of the sky unrelated to the Coma cluster and are thus more representative of the field galaxy population.

Plate 133 is the only Coma plate that has been observed during the SDSS spectroscopic commissioning phase; Coma will be re-observed as part of the main SDSS spectroscopic and photometric survey in the coming years. These data will be far superior to the data discussed herein.

5. Data Reduction

In normal production mode the SDSS will reduce the spectroscopic data through a specifically designed pipeline (Frieman et al 2001; in preparation). However, due to the uniqueness of these observations and the non-standard observing set-up, the Coma observations were processed using a modified version of an earlier copy of the spectroscopic pipeline. The reduction stages are, nevertheless, standard in multi-fiber spectroscopy. The blue and red camera data were reduced separately given the aforementioned problem with the red camera.

First, we subtracted the bias signal using the overscan columns at the edge of the CCD and co-added the individual 2-dimensional images, rejecting cosmic rays in the process. We then traced the fibers and optimally extracted the 1-dimensional spectra using the Horne (1986) algorithm. In the red this procedure had to be individually supervised and sometimes changed for troublesome fibers. No flat-fielding of the data was possible given the lack of uniformly illuminated exposures either for the whole CCD (2-dimensional flat) or through the fibers (1-dimensional flat). We wavelength calibrated the spectra using the sky emission lines. In the blue, we used the Hg, [OI] and NaD lines, while in the red, we used the numerous OH lines as well. We fitted a third order polynomial to the wavelength dispersion, and in the blue we obtained residuals of $< 0.1 \text{ \AA}$ for most fibers. For a few fibers, we did witness residuals of 0.2 \AA (which is $\simeq 15 \text{ km s}^{-1}$). However, these errors are computed at the position of the sky lines and are therefore, probably under-representative of the wavelength calibration error for the whole spectrum (see later). We obtained a similarly accurate wavelength solution in the red. On average, the blue spectra spanned the wavelength range 3770 to 6100 \AA with a median dispersion of 1.14 \AA/pix , while in the red, we obtained a wavelength coverage of 5770 to 9120 \AA with a median dispersion of 1.64 \AA/pix . These are close to the original design specification.

To sky-subtract the spectra, we combined the dedicated sky fibers into one “super-sky” spectrum which was rebinned to the resolution of the individual spectra and subtracted from each science fiber. As we did not possess calibration frames, and given the poorer quality of the red side, we did not attempt to merge the red and blue spectra. For the rest of the paper, except on the galaxy classification in Section 7 when we use $\text{H}\alpha$, we only use the blue camera data.

To correct for the intrinsic response of the instrument in the blue, we have used bright, early-type stars observed as part of the plate 133. This was achieved by selecting all stars of a spectral type earlier (hotter) than K0 which also possessed a signal-to-noise ratio per pixel of greater than 100 at 5000 \AA . In total, this criterion provided 15 stars, the earliest type being a A9-F0 star, the latest a K0. We divided these stars by the best fit stellar

template in the Jacoby et al. (1984) stellar atlas. We smoothed, normalized, and combined the resulting spectra to obtain the response function of the instrument. We then divided all the spectra by this response function. We note this procedure does not provide an absolute spectrophotometric calibration; it only corrects for the response function of the instrument.

6. Redshift Determinations

We first determined the redshifts of our spectra via visual inspection and fitted Gaussians to all obvious absorption/emission lines. The main absorption lines used were CaII H and K (3968 Å & 3934 Å), CaI (4227 Å), the Balmer series lines, MgI (5167 Å, 5173 Å & 5184 Å) and NaD (5790 Å & 5796 Å). In emission we used [OII] (3727 Å), the Balmer series lines and [OIII] (4959 Å & 5007 Å). Our visual inspections of the spectra revealed 196 galaxies in the Coma cluster, 49 field galaxies, 5 quasars, 47 stars and 12 spectra that could not be classified. The remaining 11 fibers were sky fibers.

We also used the cross-correlation technique to obtain a more accurate galaxy redshift. We utilized the RVSAO package (Kurtz & Mink 1998) within the IRAF environment. Given that the majority of synthetic spectra have resolution coarser than our data, we decided to construct our own templates for the cross-correlation using the stellar objects observed on Plate 133; this ensures that we have the same resolution for both the template and object spectra. We chose to use as templates the fifteen stars discussed above (for correcting the response function of the instrument) as well as two additional later-type stars (K1 and K4) that also passed the aforementioned signal-to-noise criterion. We also added emission lines to these stellar templates creating a set of 34 templates *i.e.*, 17 absorption line stars and 17 absorption and emission stellar templates. All templates were shifted to their rest-frame.

To determine the true error on our wavelength solutions and thus our redshifts, we first re-calculated the wavelength solution for each of our stellar templates using at least 9 lines, and normally 14, per spectrum. The availability of more lines, and the better sampling of the wavelength range, allowed us to improved the wavelength solution compared to that derived from just the sky lines alone. We then cross-correlated these re-calibrated stellar templates against higher-quality stellar spectra taken by the SDSS in later commissioning observations in Spring 2000. From these tests, we estimated that our dispersion solutions had an error of $\simeq 30 \text{ km s}^{-1}$ which we added in quadrature to the error resulting from the cross-correlation technique.

In Figure 4, we present the redshift distribution of the 245 galaxies for which we obtained a redshift on plate 133. The Coma cluster can be clearly seen as the broad peak around

$z = 0.0232$. Figure 5 is an expanded view of this region together with a $3\text{-}\sigma$ clipped Gaussian fit to the data. Cluster membership is easily assigned for our galaxy sample since there is only one galaxy in the 3 to 4σ region of the distribution. This galaxy would not normally be assigned to the cluster based on our data alone, however, CD96 measured a higher number of galaxy redshifts obtaining a larger velocity dispersion which would put this galaxy inside our $3\text{-}\sigma$ cut. Therefore, for the rest of our analysis, we included this galaxy as a cluster member, bringing the total number of Coma member on plate 133 to 196.

Table 1 lists the main galaxy data on our Coma galaxies. Column 1 gives the extraction ID number (running from 1 to 320) while Column 2 is the GMP83 number when appropriate (three of our galaxies do not have a corresponding GMP83 detection). Columns 3 and 4 give the right ascension and declination of the fiber center (not necessarily the galaxy centroid). In column 5 we present the cross-correlation redshift corrected to the heliocentric reference frame. The redshift error, in Column 6, includes the error in the wavelength calibration combined in quadrature with the error resulting from the cross-correlation technique. The usual R cross-correlation coefficient is listed in column 7. In most cases, we simply chose the cross-correlation redshift with the largest R value out of the 34 possible template cross-correlation redshifts. There were a few cases where the best R was in clear disagreement with our visual redshift measurements and in these cases we re-inspected the spectrum and quote, as our final redshift, the template with the highest R coefficient consistent with our visual redshift. These rare cases were typically due to non-corrected cosmic rays or sky residuals that produced a confident cross-correlation with one of the emission-line templates. Finally, in Columns 8 and 9, we provide the magnitudes for the galaxy taken from the SuperCOSMOS catalog and calibrated to the GMP83 system.

We have compared our redshift measurements to the data available in the literature. We have matched our catalog with the redshift compilation of CD96 as well as data from the NED²³ database. We found 151 galaxies that match previous known redshifts. The remaining 45 galaxies, approximately a quarter of our Coma redshifts, represent new measurements. In Figure 6, we show the comparison between our redshift measurements and those in the literature. The solid histogram represents the 151 matches, where 148 come from the compilation of CD96 (including their own measurements and values in the literature), and the other three are taken from NED. The solid histogram is a Gaussian fit to the entire distribution. The fit is poor because of the extended tails. We can improve the fit considerably if we reject $3\text{-}\sigma$ outliers (15 galaxies; see Figure 6). We attribute these outliers to the heterogeneity of the data where different data sets from the literature have different

²³NED is the NASA/IPAC Extragalactic Database, operated by the Jet Propulsion Laboratory, Caltech, under contract with NASA

calibration errors. Also, these discrepancies could be in part attributed to the internal dynamics of the observed galaxies because of the different fiber and/or slit placements. We can improve the fit even further by restricting ourselves to the largest homogeneous dataset from the literature *i.e.*, the 63 new redshifts measurements of CD96. We then find excellent agreement between our measurements (the dotted histogram and Gaussian fit) with a mean offset of 3 km s^{-1} and an RMS scatter of 24 km s^{-1} . Overall, the agreement of our redshift determinations with the literature is remarkably good. The RMS scatter between datasets indicates that our estimate of the errors in the wavelength calibration is accurate.

7. Spectral Classifications

In this section, we consider the spectral classification of our Coma galaxies. We have investigated four different algorithms, all of which could be implemented for the main SDSS galaxy survey. The first algorithm is based on visual inspections of the spectra but quantified using measurements of the equivalent widths²⁴ of the lines seen in the spectrum. The next two algorithms, Wavelets and Principal Component Analysis (PCA), were used to objectively classify the spectra using the visual inspections to define relevant thresholds in wavelet and eigenspace. The final classification scheme attempts to define a physical classification scheme based on synthetic models of galaxies.

7.1. Line Strength Classifications

We started by visually classifying the spectra into five classes which could then be compared to the other algorithms. We first divide the spectra into two broad classes: emission and absorption line galaxies. Absorption line spectra were then sub-divided into normal absorption line systems and objects with strong Balmer lines or post-starburst galaxies. The spectra showing emission lines were sub-divided into three categories depending on the strength of the emission lines.

For our visual and line-strength classification scheme, we were able to use both the blue side of the spectrum and the presence of $H\alpha$ in the red end of the spectrum. Unfortunately the other classification algorithms could not use the red side of the spectrum due to the condensation problems discussed above. Since $H\alpha$ is a powerful indicator of star-formation,

²⁴All equivalent widths given in this paper follow the following convention unless otherwise stated: Absorption line equivalent widths are positive and emission line equivalent widths are negative.

we believe that one of the classification schemes should utilize these data even if the others could not. Moreover, the other algorithms used our line strength classifications to quantify star-formation in Coma and therefore, it was justified to make the line strength classification as strong as possible by using all data available.

Using our equivalent width measurements, we divided the spectra in the five following types: 1) Absorption line galaxies (**AB**) which have spectra without H α in emission and with the sum of the equivalent widths of H δ , H γ and H β smaller than 15 Å. 2) Post-starburst galaxies (**PS**) which have no H α in emission, $EW(H\alpha) > 0$, and $EW(H\delta + H\gamma + H\beta) > 15$ Å. 3) Absorption line dominated galaxies but with H α in emission and modest H β emission (**AB+EM**): $EW(H\alpha) < 0$ and $EW(H\beta) > -5$ Å. 4) Emission and absorption line galaxies (**EM+AB**) which we define using $EW(H\alpha) < 0$ and $-5 < EW(H\beta) < -15$ Å. 5) Emission line dominated spectra (**EM**) which have $EW(H\alpha) < 0$ and $EW(H\beta) < -15$ Å. We present these classifications in Table 2 where Column 1 is the same extraction number as given Table 1, Column 2 is the classification based on the line strength criteria given above, Column 3 is the PCA classification and Column 4 is the wavelet classification (see below). The results of the synthetic model fitting and the parameters of the PCA classification, both of which are discussed below, are listed in Columns 5 through 10 and Columns 11 through 16, respectively.

In Figure 3, we show the distribution on the sky of the 196 galaxies given in Tables 1 and 2. The half circle shape observed on the data is due to the availability of only one spectrograph. The presence of the NGC 4839 group is obvious in the southwest region of the cluster. The plotting symbols reflect the 5 different galaxy types defined above.

7.2. Principal Component Analysis

To quantify the visual classification discussed above, we have implemented a Principal Component Analysis (PCA) of our Coma spectra (Mittaz et al 1990; Connolly et al 1995). The basis of this method consists of describing a multi-dimensional distribution of variables with a minimum number of dimensions. In our case, we are searching for the minimum number of eigenspectra needed to describe the whole spectral dataset. We can thereafter classify each spectrum as a function of these eigenspectra. We have used here a version of the official SDSS spectroscopic reduction software which already implements the PCA analysis of Connolly et al. (1995).

7.2.1. Data Preparation

As mentioned before, only the blue spectra were used for the PCA analysis. To prepare the spectra, we first interpolated over the [OI] (5577 Å) and NaD doublet (5890-5896 Å) sky emission lines since many of the spectra contained significant residuals of these strong sky lines. Next, each spectrum was blueshifted to the galaxy’s restframe and rebinned to the wavelength range 3750 → 5900 Å at a dispersion of 1.125 Å per pixel. Because of the uncertainties in the calibration (see section 5), we subtract the continuum from the spectra using a fourth order polynomial. Finally, we smoothed each spectrum with a Gaussian with a width set by the spectrograph resolution of $R = 1800$ which produced a set of 673 pixel spectra, binned over a common wavelength range, which could then be used as input to the PCA algorithm.

7.2.2. Eigenspectra Derivation

Using these prepared spectra, we performed the PCA methodology presented in Connolly et al (1995) and Connolly & Szalay (1997). We present a very brief summary below, but for a more detailed description see Connolly et al (1995). We regard each spectrum as a vector, f_λ , where λ is an index running on wavelength. We represent the whole spectra set by a matrix $f_{\lambda,i}$, where the index i runs through the individual spectra. We apply a uniform normalization to each spectrum, so that the weighted sum of the squared flux is unity. Thus, our normalized spectra are computed as

$$F_{\lambda,i} = \frac{f_{\lambda,i}}{\sqrt{\sum_{\lambda} f_{\lambda,i}^2 W_{\lambda}}} \quad (1)$$

In all cases a uniform weight was applied, so that $W_{\lambda} = 1$ for all wavelengths λ . We want to construct an orthogonal basis for the space spanned by the spectra, which we call eigenspectra. We derive these eigenspectra by diagonalizing the correlation matrix C_{ij} , given by

$$C_{ij} = \sum_{\lambda} F_{\lambda,i} F_{\lambda,j} W_{\lambda} \quad (2)$$

By diagonalizing the correlation matrix, we find the matrix R that produces the diagonal matrix Λ whose components are the eigenvalues, γ_i , of the orthogonal eigenspectra, $e_{\lambda,i}$,

$$R^\dagger C R = \Lambda \tag{3}$$

$$\begin{aligned} R_{i,j}^\dagger \left(\sum_{\lambda} F_{\lambda,i} F_{\lambda,j} \right) R_{i,j} &= \Lambda_{i,j} \\ R_{i,j}^\dagger F_{\lambda,j} F_{\lambda,j} R_{i,j} &= e_{\lambda,i} e_{\lambda,j}^\dagger = \gamma_i \delta_{i,j} \\ \Rightarrow R_{i,j}^\dagger F_{\lambda,j} &= e_{\lambda,i} \end{aligned} \tag{4}$$

In Figure 7, we show the distribution of the first 20 eigenvalues. The two curves are the percentage contribution of the N^{th} eigenvalue (decreasing curve on a log scale) and the percentage contribution of all the eigenvalues less than or equal to N (the increasing curve on a linear scale). As one can see the relative contribution of each eigenspectrum falls off rapidly; it is possible to account for $\sim 90\%$ of the variance in our sample using a reasonably small number of eigenspectra (≤ 10). The remaining $\sim 10\%$ of the variance is probably mostly noise in the data, but may also partly be due to complex, real variations in the galaxy spectra. Following the methodology of Connolly et al. (1995), we limit our classification to the first three components, as these eigenspectra contain virtually all the usable information, from a classification standpoint, as we will illustrate below. In our analysis, these three components account for 87% of the variance in our sample. By contrast, the first 2-3 components for eigensystems derived from synthetic spectra (e.g. Connolly & Szalay 1997, Ronen et al. 1999), generally account for 98-99% of the variance, while the preliminary eigensystem derived for the 2dF Galaxy Redshift Survey (Folkes et al 1999) contained about 66% of the total variance within the first three components. Our galaxy sample lies between these two extremes in terms of complexity and signal to noise, so this result is qualitatively consistent with these other works.

These first three eigenspectra are displayed in Figure 8. The first eigenspectrum represents the mean spectrum in our sample, so as expected it is a typical elliptical galaxy spectrum. It has spectral features typical of an old stellar population *e.g.*, the strong absorption lines of Ca II H & K, G band and magnesium. The second eigenspectrum contains strong Balmer absorption and emission lines, and strong [OIII] emission. This component will clearly correlate with current star formation. The third eigenspectrum again contains strong Balmer absorption, but now the strong H β and O[III] lines are shown in absorption. The eigenspectra for eigenvalues beyond the top three components do not show major spectral features, so we believe these are mostly shaped by the noise in the data. Also, the eigencoefficients for these higher order components do not show any significant trends with our visual spectral types above.

7.2.3. Galaxy Classification

The eigensystem can be used to define eigencefficients for each galaxy spectrum, which are simply the dot products of the galaxy spectrum with each eigenspectra. Since we are using uniform weights, the relationship is straightforward. For example, the i^{th} eigencefficient of the j^{th} galaxy spectrum is simply:

$$c_{i,j} = \sum_{\lambda} e_{\lambda,i} f_{\lambda,j} \quad (5)$$

The resulting set of coefficients are normalized such that ($\sum c_i^2 = 1$). In Figure 9, we show the distribution of the first, second and third eigencefficients. Immediately one can see that the different spectral types cluster into specific areas of eigenspace. The relationship between the three eigencefficients is best related by using a projection scheme as in Connolly et al. (1995), where three coefficients are converted into spherical coordinates. By assuming that all the useful information is contained within the first three components, we throw away the remaining coefficients and then treat the three top coefficients as a vector in a three dimensional space and convert them into a spherical coordinate system. In this view, the spectra can be described very simply by the two spherical angles θ and ϕ (see Figure 10). The relative lengths of the vectors are not important for classification, since they only represent how well each spectrum is represented by the three components.

Figure 10 shows the distribution of projected angles. The dashed lines show where we have made cuts based on the aforementioned classifications except that we have merged the **EM+AB** and **EM** types into one class. In figure 11, we show the composite spectra from each of our four remaining classes (these composites are simply averages of the spectra). The cuts we have made in Figure 10 are arbitrary and were chosen to reproduce the line strength classification scheme. The spectra have a continuum of possible shapes, which follow as a function of these parameters. Figure 10 shows that the angle θ correlates with the strength of the Balmer features in absorption and therefore can be used to differentiate post–starburst galaxies. The angle ϕ correlates with the emission line strength and the K–star spectral features thus being a good discriminator of the overall star formation activity. The dependence on the K–star spectral features can be seen in Figure 11 where we investigate a further division of the **AB** class into two sub–groups **ABa** and **ABb**, along a line parallel to the **PS** boundary. The **ABb** class have stronger Balmer absorption but weaker MgI and G band features than the **ABa** type.

We present the PCA classifications in Column 3 of Table 2. For completeness, we also provide the coefficients of the PCA used in this paper: Columns 11 to 13 contain the top

three eigencoefficients, Columns 14 & 15 are the θ & ϕ angle coefficients, and the square of the radius for each spectrum is given in Column 16.

7.3. Wavelet Classification

In addition to the PCA analysis on the Coma spectra, we have also investigated the use of Wavelets, since they provide a multi-resolution approach of classifying spectra that allows us to study – in a single analysis – both the small-scale emission/absorption features together with low-frequency continuum information. The goal of our wavelet analysis was to automate the line strength classification given above using as few a number of wavelet coefficients as possible thus providing an overall compression of information as well as producing an objective classification scheme that could be replicated elsewhere. For the analysis discussed herein, we have used the IDL Wavelet Workbench²⁵. We do not provide here a detailed explanation of the theory behind Wavelet since there now exists a large volume of literature on this subject (see, for example, Press et al. 1992).

To prepare the data for our wavelet analysis, analogously to the PCA analysis, we first shifted all spectra to the galaxy’s rest-frame and define a common (rest-frame) wavelength range ($3890 \rightarrow 5901 \text{ \AA}$) which only uses data from the blue side of the SDSS spectrograph. We then computed the average pixel value for the whole spectrum and subtracted this off each pixel thus re-normalizing the spectrum to have a mean of zero. This procedure removed the large discontinuities at the ends of the spectrum. The final step was to “zero-pad” the spectrum on either side of the data to create a pixel array with an integer power of two (2048 in this case). We then applied cosine-bell smoothing to the edges of the original spectrum to gradually taper the original data to zero thus avoid sharp edge-effects at the ends of the spectrum which would result in “ringing” or the Gibb’s phenomena. For our spectra, we smoothed 5% of the original data at either end of the spectrum.

We note here that as in the PCA analysis above (Section 7.2), we did not use the red side of the spectrum because of the problems discussed in Section 4 and thus we have no information about $H\alpha$ in emission. However, for the wavelets, we did retain the shape of the continuum which is different from the PCA analysis. These differences may lead to some inconsistencies in the classifications between the three techniques.

We then performed a wavelet transform on these spectra which returned a series of

²⁵Based on Wavelab at Stanford University by Donoho, Johnstone, Buckheit, Chen & Scargle. See ftp.rsinc.com/pub/user_contrib/wwb

wavelet coefficients at ten different resolution levels; the number of resolution levels is set by the size of the padded data array since each level has a factor of two lower resolution than the previous layer. An example of such a wavelet transform for one of the SDSS Coma spectra is shown in Figure 12 along with the different resolution levels and the corresponding amplitude of the wavelet coefficients at those resolution levels.

The first decision faced in the implementation of our wavelet analysis was the choice of the Mother Wavelet *e.g.*, a Daubechies, Symmlet or Coiflet wavelet function. Moreover, we also needed to choose the level of smoothness for these wavelets *e.g.*, Daubechies2 (which is just a Haar Wavelet), Daubechies4, Daubechies8 *etc.*, with the higher numbered wavelets being smoother versions of the Mother Wavelet. To aid in these decisions, we performed a series of empirical tests on the data to determine which wavelet provided the maximal compression of the information for the smallest number of coefficients used in the reconstruction of the data. In these tests, we re-constructed the spectra using the largest N coefficients (in absolute value), regardless of which level they were taken from, as well as implementing the hard thresholding scheme *i.e.*, all coefficients below the N largest-valued coefficients were set to zero in the re-construction.

In Figure 13, we show the measured mean χ^2 for all 196 Coma spectra as a function of N , the number of wavelet coefficients used in the reconstruction of the spectra. For our thresholding scheme, the Daubechies4 wavelet provided the most information compression, or largest fractional change in χ^2 , for a given N coefficients. As expected, the χ^2 decreases exponentially as a function of N , and for small values of N , the Daubechies4 clearly provides significant gain over the Symmlet wavelets. Therefore, we have used this Mother Wavelet (Daubechies4) in our analysis of these SDSS Coma spectra. This Mother Wavelet is rather sharp compared to the other wavelets which is an advantage for quantifying sharp discontinuities in these spectra *e.g.*, the 4000 Å Balmer break discontinuity.

In Figure 14, we plot the amplitude of the second and third largest wavelet coefficients for all 196 Coma spectra presented in Table 1. We have ignored the largest wavelet coefficient since it simply measures the amplitude of the whole spectrum and thus contains no information about the general shape the spectrum (this is because a wavelet is defined to sum to zero). Figure 14 demonstrates that we can extract worthwhile information about these spectra from just two of wavelet coefficients; galaxies with recent star-formation, as indicated by the presence of emission lines or post-starburst characteristics (A star spectrum), preferentially possess large (negative) second and third wavelet coefficients, while absorption, non-star-forming, galaxies populate the remainder of the phase space. The explanation for Figure 14 is that these two wavelet coefficients are measuring the “color” of the continuum and are providing a similar discrimination as one may obtain from broadband

multi-color photometry. This is exemplified by the fact that all the post-starburst galaxies in Figure 14 reside in the low-left arm since they all have “blue” spectra. In Figure 16, we show one of the post-starburst galaxies in Coma along with the re-constructed spectrum based on the three largest wavelet coefficients which illustrates that we have just measured the tilt of the spectrum. In this case, we have not exploited any high-frequency emission or absorption features, but have still managed to broadly segregate the galaxies based on their recent star-formation histories.

To extend our analysis further, we have exploited the multi-resolution nature of wavelets by designing an algorithm to classify galaxies as emission line, post-starburst and absorption line galaxies using as few a number of wavelet coefficients as possible. Here, we have merged the different sub-divisions of the emission lines as discussed in Section 7.1 and focus on the **AB**, **PS** and **EM** classes. To help define our algorithm, we co-added all the obvious post-starburst (**PS**) Coma galaxies (based on our visual classification scheme) and identified the strongest features in that co-added spectrum. In Figure 15, we show this summed spectrum and, as expected, the Hydrogen Balmer absorption series is strong because of the young A stars in the galaxy. Also visible are the Calcium H & K absorption features (with the 4000Å break Balmer discontinuity) which is indicative of an older stellar population (K star spectrum). As discussed by Dressler & Gunn (1992) and Zabludoff et al. (1996) these post-starburst galaxies are also known as E+A or K+A galaxies *i.e.*, Elliptical plus A star or K plus A star spectra.

The algorithm we have adopted is as follows. For each spectrum, we first scanned for the presence of any emission lines. This was empirically found to be equivalent to having one of the eight largest coefficients be a negative value located in the first five resolution levels *e.g.*, levels with more than 32 wavelet coefficients per level. We further restricted the search to look at wavelengths $> 4000 \text{ \AA}$ thus avoiding problems with the Balmer discontinuity.

To identify post-starburst galaxies, we then re-scanned the first twelve largest coefficients for positive wavelet coefficients near to the wavelengths of H δ , H γ and H7 (see Figure 12 for an example of this algorithm). These features were used since they are the strongest of the Balmer absorption lines as shown in Figure 15. We did not use H β because of possible contamination from emission especially if H α is present about which we have no information in the current application of the method. If three such coefficients were detected, the galaxy was defined to be a post-starburst galaxy. We present these automated classifications in Column 4 of Table 2.

7.4. Synthetic Models

As a final test, we have fit synthetic models of galaxy stellar populations to the Coma spectra. The advantage of this approach is that the spectra can be directly related to physical phenomena and parameters. The disadvantage is that the parameterization of the model, *e.g.*, initial mass function (IMF) or the star formation history of the stellar population studied, can differ substantially from the real star formation processes thus introducing large uncertainties based on the particular model used. Moreover, it is difficult to compare this scheme to the aforementioned three empirical classification schemes. Despite these caveats, we present this work here which will be primarily used in a forthcoming companion paper.

Our method for comparing the stellar models with our Coma spectra is to minimize the following χ^2 function,

$$\chi^2(a_j) = \sum_{i=1}^n \left(\frac{(F_{i\text{ observed}}^\lambda - F_{i\text{ model}}^\lambda(a_j))}{\sigma_i(F_{i\text{ observed}}^\lambda)} \right)^2 \quad (6)$$

where a_j are the free parameters of the synthetic spectrum being fitted, i is an index running through pixels, $F_{i\text{ observed}}^\lambda$ and $F_{i\text{ model}}^\lambda(a_j)$ represent each pixel of the spectral energy distributions observed and modelled respectively and $\sigma_i(F_{i\text{ observed}}^\lambda)$ the error of the observed spectrum in pixel i .

In practice, the synthetic spectral energy distributions (SEDs) have a lower spectral resolution than our observed Coma spectra. Thus, we smooth both energy distributions to the same resolution; this means that the errors of the observed spectrum are therefore no longer uncorrelated. We also mask the spectral regions around strong sky emission lines to avoid the residual spikes coming from sky subtraction.

We used two sets of synthetic spectral energy distributions. First, we employed the evolutionary synthesis model PEGASE (Fioc & Rocca-Volmerange 1997) to generate the model spectra. We minimized the χ^2 using three free parameters: an overall normalization, the age of the stellar population and the star formation prescription. We assumed solar metallicity and did not fit for the internal extinction. The star formation prescription was parameterized using two different laws: 1) we assumed that the star formation rate (SFR) depends on the galaxy gas fraction as $\Phi(t) = \nu f_g(t)$ and we minimized with respect to the astration rate ν . In fact, we minimized this astration rate parameter using 8 discrete values. Following Fioc & Rocca-Volmerange, we used the Rana & Basu (1992) IMF and values of the astration parameter that reproduce the colors of the different spectral type galaxies observed locally. We also added a one Gigayear starburst model. 2) we assumed an exponential SFR law $\Phi(t) = \tau^{-1} \exp(-t/\tau)$ and minimized with respect to the time scale τ .

In this case, we used a standard Salpeter IMF with lower and upper mass limits of 0.1 and 120 M_{\odot} , respectively.

The age and star formation prescription of the best fitting model spectrum are presented in Table 2. For the first SFR prescription we provide the age (Column 5), the number of the best fitting model (Column 6) and the reduced χ^2 (Column 7) of this best fit. The numbering of the models presented in Column 6 is the following: number 1 corresponds to a one Gigayear starburst model; numbers from 2 to 8 correspond to decreasing values of the astration rate parameter ν , where large ν values resemble star formation histories typical of early-type galaxies and small ν values, typical of late-type galaxies. The degrees of freedom of the fit depend on the actual masking of each spectrum but for the majority of them, there are 2005-2020 d.o.f. We note here that our figure of merit, the χ^2 we compute, does not strictly behave as a real χ^2 distribution. It is certainly close to one, but not exactly given that our errors have not been determined with high accuracy and there has been some smoothing which we have neglected not taking into account the correlated nature of the errors. For the second SFR prescription, we present the age (Column 8), the time scale τ (Column 9) and the reduced χ^2 (Column 10).

8. Discussion and Conclusions

8.1. SDSS Spectroscopic System

We present in this paper the first extra-galactic spectroscopic data taken by the SDSS during the initial spectroscopic commissioning run in June 1999. Although the data was primarily obtained to commission all the SDSS spectroscopic subsystems (guider, plug-plates, spectrographs, control software), and are therefore far from the nominal quality expected for the SDSS when it is fully operational, these Coma spectra are of reasonable quality and provide a new insight into the galactic content of the Coma cluster, especially at large distances from the cluster center. This is a combination of the high throughput of the SDSS spectrographs, the large field of view of the spectroscopic observations (3° diameter), the extensive wavelength coverage and resolution, and the ability to obtain many hundreds of spectra simultaneously. This single plug-plate observation of Coma illustrates the overall efficiency of the SDSS spectroscopic system and demonstrates the potential for further cluster and field galaxy observations.

As of October 2000, the entire SDSS spectroscopic system has been tested and commissioned. Both spectrographs are operational and are routinely collecting data. The target selection procedure, from determining target objects through to drilling plug-plates and ship-

ping them to APO, has been exercised several times and the emphasis has now shifted to improving the overall efficiency of the observations. At the timing of writing, the SDSS has obtained $\simeq 50,000$ spectra (approximately two thirds galaxies and one third quasars) and these data are being used, amongst other things, to define our integration time, completeness limits as well as debug the SDSS spectroscopic software. These data also represent one of the largest samples of galaxies and quasars presently in existence and are being used for several scientific programs.

We have obtained 320 spectra (half the number of a nominal SDSS plug-plate) in the central region of the Coma cluster. The availability of one spectrograph only allowed us to observe the South half of plate 133 (see Figure 3). Other engineering tasks and bad weather conditions prevented us from obtaining further Coma spectra and future data taken in this region will be acquired as part of the regular SDSS survey (both imaging and spectroscopy). Nevertheless, in one hour of observations with only half of the spectroscopic system commissioned, and without optimizing the target selection, we obtained 196 spectra of Coma galaxies. This number represents approximately $\frac{1}{3}$ of the number of redshifts presently available in the literature within the same 1.5 deg radius from the cluster center (as estimated from the NED database in August 2000). Amongst the 320 fibers available, 11 were placed on blank sky (to allow sky-subtraction from the rest of the fibers), while the rest of the science fibers yielded 196 Coma galaxies spectra, 49 field galaxies, 5 quasars (which were previously known and targeted on purpose), 47 stars and 12 unidentified spectra. Four of the unidentified spectra were due to “spill-over” from bright adjacent fibers²⁶. We note here that our target selection attempted to maximize the number of available galaxy targets by including all candidate galaxies *i.e.*, galaxies that were only classified as galaxies on one of the two photographic plates scanned by SuperCOSMOS. In hindsight, this produced considerable stellar contamination even at bright magnitude, but does ensure a higher level of completeness.

Of the 196 Coma redshifts obtained, 45 represent new identifications. Because of the SDSS large, circular field-of-view, these new redshifts are located at large cluster radii in areas scarcely sampled by other spectroscopic surveys of Coma, *i.e.* the difference between a survey instrument and a more targeted observation focused on a particular science goal. Given this uniformity, and the quality of our data, we are thus able to obtain a better understanding of the spatial distribution of galaxy classifications within Coma.

²⁶ Fibers are only separated on the CCD camera by approximately 6 pixels. The FWHM of a fiber on the CCD is approximately 2 pixels. Therefore, the light from bright target fibers can *contaminate* adjacent fibers.

For the 151 redshifts found in common with the literature, we found a negligible mean offset between our redshift determinations and those already published. In particular, when we compared our redshifts to the largest homogeneous sample of redshift available in the literature, the 63 galaxies measured by CD96, we find only a 3 km s^{-1} mean offset with an RMS scatter of only 24 km s^{-1} (this is less than 2 SDSS spectrograph pixels). This is remarkable given the non-optimal observing conditions, the lack of proper calibration frames, the difference in the spectral resolutions of the two instruments used, as well as the non-standard wavelength calibration used. Moreover, we have looked for correlations between the observed difference between CD96 and our redshift as a function of CCD position, plate position and matching distance and find no significant dependences with these observational parameters. In summary, it is likely that we have over-estimated the error due to our wavelength calibration given the low RMS difference with CD96; the SDSS spectroscopic systems appear to be remarkably stable and linear over a one hour observation.

8.2. Dynamics and Spectral Classifications

In Figure 5, we show the redshift distribution of our 196 Coma members which is qualitatively similar to that seen for the 465 redshifts in CD96 (their Figure 5). This is not surprising since we have 148 galaxies in common with their analysis. However, we do sample out to larger radius than CD96 and the fraction of galaxies measured in the NGC 4839 group (in the SW portion of the cluster), with respect to the total, is larger in our sample than in CD96. A single Gaussian fit to our data gives a mean velocity of $6950 \pm 66 \text{ km s}^{-1}$ and a velocity dispersion of $\sigma_v = 916 \pm 50 \text{ km s}^{-1}$, where we have corrected for the fact that we measure the velocity dispersion with a $3\text{-}\sigma$ clip criterion. These values are in agreement with previous measurements and, as expected, are an average of the mean velocities, and mean velocity dispersions, of the main cluster core and the NGC 4839 group (see CD96). As already noted by CD96, a single Gaussian fit to the data is an over-simplification with a clear excess of galaxies, compared to the single Gaussian, between $\simeq 6950 \rightarrow 7600 \text{ km s}^{-1}$ due to the NGC 4839 group. The central velocity of these excess galaxies is approximately coincident with the mean redshift quoted by CD96 for the NGC 4839 group, 7339 km s^{-1} . We have also investigated the dynamical differences between the absorption line galaxies and the active (emission-line and post-starburst galaxies) galaxies. We find that the **AB** galaxies given by the line strength classification have a mean velocity of $6923 \pm 70 \text{ km s}^{-1}$ and a velocity dispersion of $\sigma_v = 846 \pm 54 \text{ km s}^{-1}$, while the rest of the galaxies have $\langle cz \rangle = 7027 \pm 160 \text{ km s}^{-1}$ and $\sigma_v = 1160 \pm 134 \text{ km s}^{-1}$. The velocity dispersion of the active galaxies is then 30% higher than that of the absorption line galaxies. This is similar to the difference found by CD96 for Coma and Carlberg et al (1997) when

comparing the velocity dispersions measured from the red and blue galaxies in the CNOC1 cluster survey. We defer a more detailed examination of the dynamics of the whole Coma region until the future when we have both high quality photometric and spectroscopic data from the main SDSS survey in hand.

In this paper we present several different spectral classifications for our 196 Coma galaxies. The homogeneity and quality of the data allowed us to experiment with these different classification schemes to understand their applicability to the main SDSS survey. The first classification scheme was based on the presence or absence of emission lines. In this case, the $H\alpha$ line served as the main classifier. For typical IMF and metallicities, $H\alpha$ cannot be detected in emission ~ 25 Myr after the end of active star formation. Therefore, this criterion efficiently separates galaxies with current star formation from those without. The strength of the $H\beta$ line in emission, and the strength of the $H\delta$, $H\gamma$ and $H\beta$ in absorption, are used as additional diagnostics to improve the classification (see Section 7.1). Using these specific lines, we were able to sub-divide the galaxies into 5 spectral types which we discuss below.

Soon after the termination of a star formation episode, even if it only includes a few percent of the stellar population, the blue part of the optical spectrum of a galaxy is dominated by A stars which are characterized by the Balmer absorption features. If there is no further star formation activity the strength of these lines diminishes gradually with time. The Balmer absorption lines strength thus provides a rough estimate of the age of the stellar population, although the lines are also somewhat sensitive to metallicity. We use this criterion to separate absorption line systems into two sub-classes. Galaxies without recent star formation, based on the absence of $H\alpha$ in emission and the absence of strong Balmer absorption, were classed as (**AB**). Galaxies in which their last episode of star formation ended recently, or post-starburst galaxies (**PS**), were characterized by their strong Balmer absorption lines as well as the absence of $H\alpha$ in emission. The threshold between **AB** and **PS** was set at an equivalent width larger than 15 \AA for the sum of $H\delta$, $H\gamma$ and $H\beta$ equivalent widths. This corresponds to roughly 400-700 million years after the truncation of the active star-formation for solar metallicity. We note here that our criteria are based on equivalent widths; thus this threshold also depends upon the underlying stellar population (or the previous star formation history) *i.e.*, how many stars are contributing to the continuum. Emission line galaxies were divided into three sub-classes (**AB+EM**, **EM+AB** and **EM**) depending upon the strength of the $H\beta$ line. The $EW(H\beta)$ cuts are difficult to translate into star formation rates given the different continuum strengths and the fact that we have not attempted to correct the intrinsic extinction. Nevertheless, the equivalent width of $H\beta$ represents a measure of the strength of the star formation process with respect to the underlying stellar population.

This classification scheme has the advantage of being simple and easy to measure in optical spectra with sufficient wavelength coverage, and is meaningful as it classifies spectra according to their star formation activity relative to the overall stellar population. Undoubtedly, the use of $H\alpha$, instead of $H\beta$, to subdivide the emission line spectra would have been preferred, as it is a better indicator of star formation and is less affected by extinction. However, the nature of our data made us settle for $H\beta$. We can use this classification as the test base to which compare our other schemes.

Other classification schemes based on spectral features have also been used in the literature. In particular, the MORPHS group (Dressler et al 1999; Poggianti et al 1999) and the CNOC group (Balogh et al 1999) have recently put forward similar classification schemes based on the [OII] and $H\delta$ lines, in which they provide a more physical interpretation of their types based on evolutionary spectral synthesis models. They use the [OII] and $H\delta$ lines as indicators of current star formation and the time elapsed after the last episode of star formation, respectively. The large wavelength coverage of our spectra allow us to use more spectral features, $H\alpha$, $H\beta$, $H\gamma$ and $H\delta$, for the same purpose. Here, we have taken the phenomenological approach of providing a simple classification scheme based on observational quantities which are directly related to the star formation processes taking place within galaxies. We defer to a future paper a more detailed interpretation of these classes in terms of the evolutionary phases of galaxy stellar populations.

There are 44 galaxies (22% of our sample) that show evidence of current star formation to some degree. There are five extra galaxies, classified as post starbursts, which ceased their star formation process in the last ~ 500 Myr. If we include these five galaxies into the active galaxy population, then 25% of our galaxy sample show some sign of recent star formation activity. In Figure 3, we show the spatial distribution of all 196 Coma galaxies; the plotting symbol type reflects our line strength classification scheme discussed above and in Section 7.1. Clearly, there is no obvious correlation in the position of the different types of galaxies except that the active star-forming galaxies avoid the cluster center.

In addition to the line strength classification scheme, we have explored two objective schemes based on PCA and wavelets. For our PCA analysis, Figure 7 shows that the first three eigenspectra for our dataset contains 87% of the variance while most of the remaining variance is likely due to the noise in our spectra. Each spectrum can therefore be expressed as a linear combination of these three eigenspectra which in turn can be presented in a spherical coordinate system with only two important parameters (see Figure 10). We have defined regions in this two-dimensional space according to our line strength classification scheme.

In Table 3, we compare the line strength and PCA classifications to check whether the

two-dimensional space defined by the eigencoeficient projection angles can be understood in terms of the absorption and emission lines of the spectra. The agreement between both classifications is obviously good but nevertheless remarkable as there was no a priori guarantee that such a good separation should be achieved given that the PCA classification is based on the overall continuum subtracted SED while the line strength classification only on the Balmer lines. Figure 10 demonstrates that simple arbitrary cuts can efficiently separate galaxies according to their spectral line strengths. The only cut which does not clearly reproduce the line strength classification above is the division between **AB** and **AE** galaxies. In fact this is mostly due to the fact that we have used $H\alpha$ to split these two classes in the line strength classification but have only used the blue part of the spectrum in the PCA analysis. Some of these galaxies show $H\alpha$ in emission while the rest of the Balmer series is seen in absorption. PCA thus classifies the galaxy as an **AB** galaxy while in the line strength classification it is an **AB+EM** galaxy based on the presence of faint $H\alpha$ emission. In addition, two galaxies classified as **AB+EM** by their line strengths are classified as **PS** by the PCA analysis (fibers 91 and 140). Both galaxies show strong broad Balmer absorption features which are filled with narrower emission. In these cases, it is difficult to separately measure the absorption and emission line component equivalent widths. We estimate that galaxy 91 has $EW(H\delta+H\gamma+H\beta) \sim 10 \text{ \AA}$ in absorption and galaxy 140 has $EW(H\delta+H\gamma+H\beta) \sim 15 \text{ \AA}$. The latter would have been classified as a **PS** galaxy by the line strength criteria if it did not have the emission. These two galaxies have certainly experienced star formation activity that has been substantially decreased in the last Giga-year thus giving rise to the strong Balmer absorption lines. However, there is still some residual star formation activity going on and thus the weak emission on top of the absorption.

We have also used wavelets to define a simple classification for these spectra which uses both the absorption and emission lines in conjunction with the continuum shape. As with the PCA analysis, we only utilize the blue part of the spectrum and thus have no information on $H\alpha$. We also do not try and differentiate between the **EM**, **AB+EM** and **EM+AB** line strength types since, at present, we cannot measure the equivalent width of lines directly from the wavelet analysis (although in principle this could be achieved). In Table 4, we compare the wavelet classification to the line strength classification. As above, there is good agreement between the two where the line strength sub-classes of **AB+EM** and **EM+AB** classifications are mostly shared between the **EM** and **AB** wavelet classes (19 **AB+EM** galaxies were placed in the wavelet **AB** class as expected since there is no information about $H\alpha$). The only surprises in Table 4 are the four galaxies (fibers 84, 138, 201 & 244) classified as **AB** in wavelet space but **EM+AB** by the line strength criteria. A visual inspection of these spectra shows that the signal-to-noise of these data is, on average, low. However, all four have moderately weak emission lines that probably missed

the top 8 wavelet coefficients because of their size. All four do have strong Calcium H & K indicative of an old stellar population. We also note that the wavelet algorithm has more **PS** galaxies than the line strength classification. This is primarily due to the hard threshold of $EW(H\delta + H\gamma + H\beta) > 15 \text{ \AA}$ imposed in the line strength classification. These extra wavelet **PS** galaxies (three classified as **AB** and 7 as **AB+EM** galaxies by the line strength method) do have Balmer absorption lines, but either they have $H\alpha$ in emission and/or the Balmer absorption is weak (although still stronger than galaxies dominated by old stellar populations). This apparent discrepancy in the classification schemes can be easily understood in terms of the thresholds used in assigning the **PS** classification, *i.e.* if the 15 \AA threshold used in the line classification scheme had been lowered, then many of these galaxies would have also been classified as **PS** by the line strength scheme. The wavelet scheme has simply picked extra *older* post–starburst galaxies with weaker Balmer absorption lines.

In Table 5, we show the cross-comparison between the PCA and wavelet classifications. Again, the agreement is very good. The only exceptions are the same cases discussed above given that the PCA classification cuts were applied to reproduce the line strength classification. It is worth mentioning here that the extra wavelet **PS** classified galaxies discussed above reside in the “bridge of galaxies” that join the **AB** and **PS** regions shown in Figure 10. This again explains why we find more wavelet classified **PS** galaxies compared to the other schemes since we are simply sampling more of the galaxy population between these two classes.

We have also fitted evolutionary spectral synthesis models to our Coma spectra (only the blue side of the spectrum) to understand the composition and history of the stellar populations in these galaxies. We note that these fits are performed for a particular model, with a chosen star formation prescription, and should be interpreted as such. The star formation history of a galaxy is more complex than the simple parameterized models used (e.g., Abraham et al 1999) and the best fit gives only an indication of the properties of the combined stellar population and helps to compress the spectral information into a handful of meaningful parameters.

We have chosen to fit the age of the stellar population and a parameter describing the star formation prescription using two families of models (see section 7.4 for further details). Both parameterizations give similar results (see table 2). It is nevertheless clear from table 2 that in some cases the star formation prescription utilized is unable to fit properly the observed spectrum and a different prescription with combinations of different bursts is necessary. We have chosen, at this stage of simple comparison with other classification schemes, not to fit for the intrinsic absorption or the galaxy metallicity, assuming fixed solar metallicity and no intrinsic absorption. Indeed, there are known degeneracies between age–

metallicity and age–intrinsic absorption when fitting synthesized SED to observed spectra (e.g., Worthey 1994; Thompson, Weymann & Storrie-Lombardi 2000). In general, a higher metallicity and the effect of neglecting internal extinction will be compensated by an older computed age.

Figure 18 presents the age and time scale, τ , of the best fit synthesized SED using an exponential SFR law. The symbols represent the different line strength classifications while the size of the symbol represented the observed magnitudes of the galaxies. Most of the Coma galaxies cluster along a strip in the age– τ space. The large dynamic range shown for the τ parameter gives the impression that galaxies of different line strength classes populate similar regions in this parameter space. However, the general trends of age– τ values with respect to the spectral line strength classification are as expected: **AB** galaxies populate regions of old ages ($\geq 3 - 4$ Gyr) and short time–scales of star formation which produce old stellar population while the **AB+EM**, **EM+AB** and **EM** galaxies occupy regions next to the **AB** galaxies but gradually moving to younger ages and longer τ as the emission lines strength increases. Finally, the **PS** galaxies populate the region of short time scale star formation, which correspond to short and intensive star formation histories, and short ages after the strong formation episode. To help visualize these separate regions of the age– τ space, we show in Figure 20 the 1, 2 and 3 σ contours of the age– τ regions occupied by three representative galaxies drawn from our three main spectral types *i.e.*, an **AB** type galaxy (fiber 143), a **PS** type galaxy (fiber 95) and a **EM+AB** type galaxy (fiber 117). It is clear from this plot that the **AB** and **EM+AB** galaxy inhabit different regions of the age– τ space (at the 3 σ level) while there is no intersection for the **AB** and **PS** galaxies either. Only the **EM+AB** and **PS** galaxies share a similar parameter space (at the 3 σ level). In summary, our spectral classifications have a broad relationship to expected physical models of star–formation and therefore, they can be used to study star–formation and galaxy evolution with the Coma cluster.

8.3. Galaxy Star–Formation in Coma

Our analysis of the Coma cluster has revealed that a substantial fraction (25%) of galaxies in Coma (out to the virial radius) exhibit recent star–forming activity. Such analyses are at the heart of studies of galaxy evolution in clusters and, in more general terms, the “Butcher–Oemler” effect (Butcher & Oemler 1984). Our large fraction of recent star–forming galaxies is more than initially expected for such a low redshift cluster but is in reasonable agreement with other spectroscopic studies of galaxy star–formation in clusters. For example, Caldwell & Rose (1997) found that $\sim 15\%$ of galaxies in five nearby clusters showed signs of

recent star-formation while the work of Ellingson et al. (2000) shows that $\sim 20\%$ of galaxies within the virial radius ($\sim r_{200}$) of CNOC1 clusters ($0.18 < z < 0.5$) show signs of recent star-formation. However, we do not address here the redshift dependence of the BO effect since that will require a large, homogeneous sample of clusters spanning a significant range in redshift (See Andreon & Etori 1999; Margoninier & Carvalho 2000). We will address this issue using the main SDSS sample.

We explore here possible mechanisms for triggering star-formation in clusters of galaxies. Several authors (Burns et al. 1994; Caldwell & Rose 1997; Metevier, Romer & Ulmer 1999; Wang, Connolly & Brunner 1997) have proposed that shocks caused by cluster merger events can trigger star-formation in cluster galaxies. However, Figures 3 and 17 show that our Coma galaxies with recent star-formation (**EM+AB, AB+EM, EM** and **PS**) are random distributed throughout the cluster with no apparent correlation with the NGC 4839 group. This implies that this merger (or post-merger) has had little effect on the recent star-formation rates of Coma contrary to the scenario outlined in Burns et al. (1994) and Caldwell & Rose (1997). This difference may be the combination of several effects: 1) We have a complete, homogeneous, spectroscopically confirmed, sample of Coma galaxies out to large cluster radii *i.e.* we have targeted all bright galaxies out to the virial radius of Coma regardless of their location, color or morphological type. Caldwell & Rose (1997) were forced to selectively sample specific areas in Coma, because of the smaller field-of-view of their instrument, as well as preferentially targeting early-type galaxies; 2) We have used different schemes, and thresholds, for defining post-starburst and star-forming galaxies. For example, if we lowered our threshold for the definition of a **PS** galaxy (to older and weaker lines) we may find a correlations with the NGC 4839 group. We note however that the extra wavelet **PS** galaxies (which are older **PS** galaxies) show no sign of excess clustering with the NGC 4839 group; 3) The NGC 4839 is approximately 5–10% (CD96) of the mass of the core of Coma and thus the merger of Coma and this group may not be severe enough to trigger the levels of star-formation seen in more extreme head-on cluster-cluster and group-group mergers (Metevier et al. 1999); 4) If the NGC 4839 group is still “spiralling” into Coma then we could simply be seeing the combination of ram-pressure induced star-formation as the field galaxies first infall into the cluster (see Dressler & Gunn 1983) as well as the expected recent star-formation in the NGC 4839 group before it fell in (see Zabludoff et al. 1996). This would also explain the large velocity dispersion measured for the emission-line galaxies (Carlberg et al. 1997). We must await further data to fully discriminate between these possible models or others. It is important to note that we only sample galaxies brighter than $b = 18$ and therefore our observations only apply to the brightest galaxy members and not to the dwarf population (see Rakos et al. 2000). Moreover, our observations do not distinguish between different morphological types (see Doi et al. 1995a,b); this will be addressed using

the main SDSS survey data.

The characteristic radius of the Coma cluster is $r_{200} \sim 1.5 h^{-1}$ Mpc (Geller et al 1999), or 1.25 degrees, and thus, we sample the galaxy population out to the virial radius and slightly beyond. This provides a unique opportunity to study the large-scale star-formation histories of galaxies in this nearby cluster. In Figure 20, we present the fraction of passive (absorption) and active (emission plus post-starburst) galaxies as a function of projected distance from the center of Coma. The azimuthally averaged fraction of active galaxies (**PS**, **AB+EM**, **EM+AB**, **EM** types) appears to increase slightly with radius from 0.15 to 1.2 degrees²⁷, but the observed percentages are also consistent with a constant radial fraction of active galaxies in this region. This trend is different from that observed in the CNOC sample at higher redshift (Ellingson et al 2000), i.e., they observe a steeper radial profile for the fraction of active galaxies in their high redshift clusters. However, the results are consistent given the errors and the different analyses performed which render a detailed comparison difficult.

We find no active galaxies in the central (projected) $\sim 200 h^{-1}$ Kpc of the Coma cluster. This result is similar to that observed by Ellington et al. (2000) who found a deficit of star-forming galaxies within $0.5r_{200}$ of the cores of CNOC1 clusters (see also Rakos et al. 2000 who found a similar trend in intermediate redshift clusters). Ellingson et al. (2000) propose that the dense intracluster medium in the cores of clusters inhibits star-formation producing a deficit of star-formation compared to the outskirts of the cluster and the general field population. Our data certainly agrees with this scenario except we do see a reduction of active galaxies beyond r_{200} , although this reduction is not statistically significant. We defer a detailed discussion of Coma’s star-forming galaxies, and their relation to the X-ray gas, to a future paper.

The Sloan Digital Sky Survey (SDSS) is a joint project of The University of Chicago, Fermilab, the Institute for Advanced Study, the Japan Participation Group, The Johns Hopkins University, the Max-Planck-Institute for Astronomy, Princeton University, the United States Naval Observatory, and the University of Washington. Apache Point Observatory, site of the SDSS, is operated by the Astrophysical Research Consortium. Funding for the project has been provided by the Alfred P. Sloan Foundation, the SDSS member institutions, the National Aeronautics and Space Administration, the National Science Foundation, the U.S. Department of Energy, and Monbusho. The official SDSS web site is www.sdss.org.

²⁷At the distance of Coma, one degree on the sky corresponds to $1.2 h^{-1}$ Mpc.

REFERENCES

- Abraham, R. G., Ellis, R. S., Fabian, A. C., Tanvir, N. R. & Glazebrook, K. 1999, MNRAS, 303, 641
- Adami, C., Nichol, R. C., Mazure, A., Durret, F., Holden, B. & Lobo, C. 1998, A&A, 334, 765
- Adami, C., Ulmer, M. P., Durret, F., Nichol, R. C., Mazure, A., Holden, B. P., Romer, A. K. & Savine, C. 2000, A&A, 353, 930
- Andreon, S., Etti, S., 1999, ApJ, 516, 647
- Balogh, M.L., Morris, S. L., Yee, H. K. C., Carlberg, R. G. & Ellingson, E. 1999, 527, 54
- Bernstein, G. M., Nichol, R. C., Tyson, J. A., Ulmer, M. P. & Wittman, D. 1995, AJ, 110, 1507
- Biviano, A. 1998, in “Untangling Coma Berenices: A New Vision of an Old Cluster”, eds. Mazure, A., Casoli F., Durret F., Gerbal D., World Scientific Publishing, p1
- Briel, U. G., Henry, J. P. & Böhringer, H. 1992, A&A, 259, L31
- Butcher, H. & Oemler, A. 1984, ApJ, 285, 426
- Burns, J. O., Roettiger, K., Ledlow, M. & Klypin, A. 1994, ApJ, 427, L87
- Caldwell, N., Rose, J. A., Sharples, R. M., Ellis, R. S. & Bower, R. G. 1993, AJ, 106, 473
- Caldwell, N. & Rose, J. A., 1997, AJ, 113
- Carlberg, R. G., Yee, H. K. C., Ellingson, E., Morris, S. L., Abraham, R., Gravel, P., Pritchet, C. J., Smecker-Hane, T., Hartwick, F. D. A., Hesser, J. E., Hutchings, J. B. & Oke, J. B. 1997, ApJ, 476, L7
- Colles, M. & Dunn, A. M. 1996, ApJ, 458, 435 (CD96)
- Connolly, A. J., Szalay, A. S., Bershad, M. A., Kinney, A. L., & Calzetti, D. 1995, AJ, 110, 1071
- Connolly, A. J., & Szalay, A. S. 1999, AJ, 117, 2052
- Doi, M., Fukugita, M., Okamura, S. & Turner, E. L. 1995a, AJ, 109, 1490
- Doi, M., Fukugita, M. & Okamura, S. 1995b, ApJS, 97, 59

- Dressler, A. & Gunn, J. E. 1983, ApJ, 270, 7
- Dressler, A. & Gunn, J. E. 1992, ApJS, 78, 1
- Dressler, A., et al., 1999, ApJS, 110, 213
- Ellingson, E., Lin, H., Yee, H. K. C. & Carlberg, R. G. 2000, ApJ, in press, (astro-ph/0010141)
- Fan, X. et al 2000, AJ, in press (astro-ph/0008123)
- Fioc, M. & Rocca-Volmerange, B. 1997, A&A, 326, 950
- Folkess, S., et al. 1999, MNRAS, 308, 459
- Fukugita, M., Ichikawa, T., Gunn, J.E., Doi, M., Shimasaku, K., & Schneider, D.P. 1996, AJ, 111, 1748
- Geller, M., Diaferio, A. & Kurtz, M. J. ApJ, 517, L23
- Gehrels, N. 1986, ApJ, 303, 336
- Godwin, J. G., Metcalfe, N. & Peach, J. V. 1983, MNRAS, 202, 13 (GMP83)
- Horne, K. 1986, PASP, 98, 609
- Honda, H., Hirayama, M., Watanabe, M., Kunieda, H., Tawara, Y., Yamashita, K., Ohashi, T., Hughes, J. P. & Henry, J. P. 1996, ApJ, 473, L71
- Hughes, J. P. 1989, ApJ, 337, 21
- Jacoby, G. H., Hunter, D. A. & Christian, C. A. 1984, ApJS, 56, 257
- Kashikawa, N., Sekiguchi, M., Doi, M., Komiyama, Y., Okamura, S., Shimasaku, K., Yagi, M. & Yasuda, N. 1998, ApJ, 500, 750
- Kent, S. M. & Gunn, J. E. 1982, AJ, 87, 945
- Kurtz, M. J. & Mink, D. J. 1998, PASP, 110, 934
- Mittaz, J. P. D., Penston, M. V. & Sniijders, M. A. J. 1990, MNRAS, 242, 370
- Margoniner, V. E., de Carvalho, R. R., 2000, AJ, 119, 1562
- Metevier, A. J., Romer, A. K., Ulmer, M. P., 2000, AJ, 119, 1090

- Nichol, R.C., Collins, C.A. & Lumsden, S.L. 2000, ApJS, submitted (astro-ph/0008184)
- Poggianti, B. M., Smail, I., Dressler, A., Couch, W. J., Barger, A. J., Butcher, H., Ellis, R. S. & Oemler, A. J. 1999, ApJ, 518, 576
- Press, W. H., Teukolsky, S. A., Vetterling, W. T. & Flannery, B. P. 1992, Cambridge: University Press, —c1992, 2nd ed.,
- Rana, N. C. & Basu, S. 1992, A&A, 265, 499
- Rakos, K. D., Schombert, J. M., Odell, A. P., Steindling, S., ApJ, 540, 715
- Ronen, S., Aragón-Salamanca, A. & Lahav, O. 1999, MNRAS, 303, 284
- Thompson, R. I., Weymann, R.J. & Storrie-Lombardi, L. J. 2000, ApJ, in press, (astro-ph/0008276)
- Wang, Q. D., Connolly, A. & Brunner, R. 1997, ApJ, 487, L13
- West, M.J. 1998, in “Untangling Coma Berenices: A New Vision of an Old Cluster”, eds. Mazure, A., Casoli F., Durret F. , Gerbal D., World Scientific Publishing, p36
- White, S. D. M., Briel, U. G. & Henry, J. P. 1993, MNRAS, 261, L8
- Worthey, G. 1994, ApJS, 95, 107
- York, D. G. et al 2000, AJ, in press, astro-ph/0006396
- Zabludoff, A. I., Zaritsky, D., Lin, H., Tucker, D., Hashimoto, Y., Sheckman, S. A., Oemler, A. , Kirshner, R. P. 1996, ApJ, 466, 104

Table 1. Galaxy Redshifts.

Fiber number	GMP83 number	RA ^a (J2000)	DEC ^a (J2000)	cz km/s	δcz km/s	R	b	r
3	1411	13 02 32.8	27 17 43	7585	39	6.9	17.36	15.47
4	1382	13 02 35.6	26 39 43	7372	72	3.0	17.97	16.04
10	1060	13 03 13.7	27 22 08	6371	32	15.7	16.84	14.88
11	1368	13 02 37.4	27 10 34	5497	33	15.4	16.52	14.65
12	455	13 04 26.6	27 18 16	5534	31	16.9	15.77	14.52
13	1392	13 02 35.2	27 26 20	5400	41	7.4	17.07	15.43
14	1635	13 02 5.5	27 17 50	7258	35	10.5	17.50	15.57
21	1245	13 02 52.7	27 51 59	8207	32	19.9	15.62	13.81
27	1134	13 03 5.2	27 47 03	7671	32	18.9	16.74	14.88
28	177	13 05 8.5	27 30 46	7177	35	10.9	17.05	15.25
29	631	13 04 4.8	27 51 01	6360	34	11.4	17.77	15.96
30	228	13 05 3.3	27 32 13	6603	61	4.3	17.88	16.21
31	1616	13 02 7.9	27 38 54	6915	33	12.4	15.45	13.74
32	1673	13 02 1.1	27 39 10	7065	32	17.6	16.61	14.70
34	595	13 04 11.2	27 29 25	5317	34	10.3	16.50	14.67
40	2235	13 01 10.7	27 14 47	6226	46	5.7	18.01	16.18
43	2278	13 01 6.2	27 23 52	8109	33	14.4	17.42	15.60
45	2639	13 00 29.2	27 19 59	8408	67	5.6	17.67	16.37
50	2643	13 00 29.2	26 40 31	7185	31	23.3	15.60	13.71
55	2431	13 00 49.9	27 24 20	6569	32	16.0	15.32	13.42
58	1681	13 02 0.1	27 46 57	7111	36	12.2	16.08	14.43
61	1961	13 01 36.5	27 42 28	7912	37	8.4	18.03	16.24
65	1832	13 01 48.4	27 36 14	8210	32	17.0	16.70	14.82
66	2219	13 01 12.3	27 36 16	7543	32	17.9	16.79	14.87
68	2385	13 00 54.8	27 50 31	7096	33	13.2	17.68	15.89
69	2157	13 01 17.6	27 48 33	7281	32	20.1	15.04	13.12
70	2347	13 00 59.3	27 53 59	6883	32	19.7	15.88	13.98
74	2355	13 00 58.4	27 39 07	5202	38	6.6	16.67	14.80
75	1807	13 01 50.2	27 53 36	7562	36	10.9	15.89	14.00
76	2185	13 01 15.2	27 40 09	7065	43	7.4	17.76	15.91
84	3143	12 59 49.3	26 58 27	7072	32	13.6	17.88	16.53
85	3618	12 59 16.7	27 06 21	8412	33	13.7	17.38	15.48
86	3622	12 59 16.4	27 09 29	6692	32	17.6	16.67	14.78
87	3310	12 59 37.4	27 20 09	6953	34	11.4	17.84	15.94

Table 1—Continued

Fiber number	GMP83 number	RA ^a (J2000)	DEC ^a (J2000)	cz km/s	δcz km/s	R	b	r
88	2987	13 00 3.5	26 53 53	5911	32	16.1	14.43	12.52
89	2948	13 00 6.3	27 18 02	7858	32	18.5	16.87	14.99
91	3100	12 59 54.4	26 49 11	7994	36	12.1	16.98	15.34
94	3661	12 59 13.7	27 24 09	5644	33	15.5	15.77	13.84
95	2640	13 00 29.2	27 30 52	7395	38	14.1	16.33	15.02
96	2945	13 00 6.3	27 46 32	6175	32	19.7	16.27	14.33
97	2615	13 00 32.5	27 45 58	6662	32	19.3	16.99	15.10
98	2599	13 00 33.7	27 38 15	7498	33	12.2	15.97	14.72
99	2776	13 00 19.1	27 33 13	5862	32	17.3	16.19	14.27
100	2721	13 00 22.4	27 37 24	7592	33	14.1	17.57	15.69
101	2393	13 00 54.7	27 47 08	8282	69	3.1	16.22	14.31
102	2603	13 00 33.4	27 49 27	8176	33	13.5	17.48	15.69
103	2942	13 00 6.3	27 41 06	7561	32	17.8	16.64	14.82
105	2783	13 00 18.6	27 48 56	5328	36	8.4	17.59	15.66
106	2582	13 00 35.7	27 34 27	5064	36	8.9	16.24	14.39
107	2894	13 00 10.4	27 35 42	5587	32	14.4	17.26	15.36
108	2866	13 00 12.6	27 46 54	7008	33	14.2	16.97	15.22
110	2601	13 00 33.6	27 30 14	5602	32	15.2	16.88	15.60
111	2688	13 00 25.2	27 33 08	7258	33	13.6	17.80	15.96
115	4106	12 58 39.9	26 45 33	7467	31	19.3	17.01	15.76
117	4135	12 58 37.2	27 10 35	7705	32	13.8	15.81	14.33
120	3837	12 59 1.8	26 48 56	7117	33	17.0	14.60	12.59
123	4206	12 58 32.1	27 27 22	7007	32	17.8	16.48	14.58
124	4192	12 58 33.1	27 21 51	6950	32	18.1	16.34	14.41
126	4159	12 58 35.4	27 15 52	7380	32	15.9	16.15	14.77
127	4351	12 58 18.7	27 18 38	7447	31	18.4	17.04	15.39
130	4147	12 58 36.3	27 06 15	7954	31	22.0	15.41	13.49
131	4294	12 58 25.3	27 11 59	8035	38	7.2	17.90	16.04
132	4124	12 58 37.9	27 27 50	6243	43	5.4	16.67	14.72
133	3238	12 59 41.3	27 39 35	6742	32	18.8	16.88	14.95
134	3298	12 59 37.8	27 46 36	6766	34	11.2	17.50	15.75
135	3296	12 59 37.9	27 54 26	8005	33	17.4	16.08	14.14
136	3165	12 59 47.1	27 42 38	8324	31	21.5	14.91	13.02
137	3400	12 59 30.8	27 53 03	4692	35	12.2	15.55	13.63

Table 1—Continued

Fiber number	GMP83 number	RA ^a (J2000)	DEC ^a (J2000)	cz km/s	δcz km/s	R	b	r
138	3271	12 59 39.8	27 34 36	5012	32	13.4	16.63	15.23
139	3178	12 59 46.1	27 51 26	8096	31	23.8	16.27	14.45
140	3071	12 59 56.2	27 44 47	8883	50	8.2	17.39	16.07
141	3092	12 59 54.9	27 47 45	8250	32	16.6	17.66	15.81
142	3423	12 59 29.4	27 51 00	6797	34	16.4	15.95	14.07
143	3201	12 59 44.4	27 54 45	6679	32	19.6	15.70	13.79
144	3510	12 59 23.2	27 54 45	6821	36	11.5	14.46	12.59
145	3557	12 59 20.2	27 53 09	6468	32	17.9	16.53	14.70
146	3012	13 00 1.5	27 43 51	8051	41	7.4	17.52	15.74
147	3493	12 59 24.9	27 44 19	6027	32	17.5	16.55	14.68
148	3313	12 59 37.0	27 49 32	6244	32	15.7	17.64	15.83
149	3403	12 59 30.7	27 47 29	7762	31	20.3	17.06	15.23
150	3262	12 59 39.9	27 51 17	3747	40	6.9	16.77	14.94
151	3339	12 59 35.3	27 51 49	6274	32	14.9	17.81	15.91
152	3126	12 59 51.0	27 49 58	7921	33	14.1	17.69	15.74
153	3730	12 59 8.2	27 47 02	7033	33	18.0	15.37	13.40
155	3588	12 59 18.5	27 30 48	6009	37	8.2	18.01	16.31
156	3829	12 59 1.6	27 32 13	8570	42	6.9	17.73	15.80
158	3739	12 59 7.4	27 46 06	6336	33	14.9	15.80	13.94
160	3958	12 58 52.1	27 47 05	5662	33	15.8	15.96	14.14
161	3660	12 59 13.5	27 46 28	6818	31	20.8	15.85	13.91
162	3697	12 59 10.3	27 37 11	5725	32	17.2	16.67	14.80
163	3879	12 58 58.1	27 35 41	5998	32	18.7	16.39	14.52
164	3997	12 58 48.7	27 48 37	5918	33	15.9	15.37	13.48
165	4017	12 58 47.4	27 40 29	8378	32	18.8	15.04	13.11
166	3782	12 59 4.6	27 54 39	6408	32	19.2	16.75	14.84
167	3943	12 58 53.0	27 48 48	5523	33	13.9	16.96	15.11
168	3779	12 59 5.3	27 38 39	5387	33	11.9	15.36	13.85
169	3733	12 59 8.0	27 51 18	6556	32	19.4	15.87	13.99
172	3896	12 58 56.1	27 50 00	7473	33	13.8	14.99	13.27
173	4522	12 58 1.5	27 29 22	7633	31	20.3	15.78	13.92
174	4502	12 58 3.5	27 40 56	7220	32	16.7	18.02	16.10
175	4447	12 58 9.7	27 32 57	6970	33	15.0	17.83	15.89
178	4579	12 57 56.3	27 34 52	4984	31	21.6	16.94	15.81

Table 1—Continued

Fiber number	GMP83 number	RA ^a (J2000)	DEC ^a (J2000)	cz km/s	δcz km/s	R	b	r
179	4209	12 58 31.6	27 40 24	6910	32	18.3	17.01	15.13
180	4255	12 58 28.4	27 33 33	7554	36	11.6	16.63	14.94
181	4469	12 58 6.8	27 34 36	7504	36	9.0	17.85	15.91
182	4156	12 58 35.2	27 35 47	7694	35	13.8	14.71	12.96
183	4060	12 58 42.6	27 45 37	8662	66	5.7	17.79	16.48
184	4348	12 58 18.2	27 50 54	7612	45	8.8	18.04	16.69
185	4117	12 58 38.4	27 32 38	5964	32	17.1	16.77	14.90
187	4083	12 58 40.8	27 49 37	6163	37	8.2	17.81	15.98
190	4341	12 58 19.2	27 45 43	5420	32	15.1	17.32	15.52
191	4499	12 58 3.5	27 48 53	7118	32	20.4	16.18	14.33
192	4314	12 58 22.0	27 53 32	7276	32	16.0	17.76	15.89
193	4731	12 57 43.0	26 51 08	6356	31	20.3	15.85	13.99
194	4793	12 57 36.5	27 01 52	7328	32	19.6	16.27	14.28
196	4582	12 57 56.7	27 02 14	7419	33	13.3	16.70	14.83
197	4518	12 58 3.2	26 54 57	8188	32	18.0	15.98	14.11
201	4463	12 58 9.2	26 39 51	7314	31	17.0	17.34	15.78
202	4912	12 57 26.7	26 41 37	7248	34	11.0	17.70	15.77
204	4692	12 57 45.7	27 25 45	8334	34	13.0	17.56	15.73
205	4479	12 58 6.1	27 25 08	5759	34	11.3	17.62	15.76
209	4918	12 57 25.3	27 24 16	4863	31	21.3	16.31	14.37
210	4535	12 58 0.8	27 27 14	7662	32	16.4	17.95	16.04
212	4961	12 57 21.5	27 01 22	8009	33	14.6	17.80	16.00
213	4928	12 57 23.9	27 29 46	7329	41	8.5	15.43	13.40
216	4714	12 57 43.2	27 34 39	7204	33	14.2	17.71	15.87
218	4829	12 57 32.8	27 36 37	6052	34	14.5	14.92	12.97
219	4794	12 57 35.8	27 29 35	7299	32	20.1	15.41	13.42
220	4907	12 57 25.8	27 32 46	5580	33	16.0	16.09	14.21
221	5051	12 57 9.4	27 27 59	7447	32	19.4	15.55	13.60
222	4597	12 57 54.4	27 29 26	4962	34	10.8	16.47	14.62
223	4933	12 57 23.5	27 45 58	9115	32	19.0	16.39	14.43
224	4653	12 57 48.1	27 52 58	5849	32	19.0	15.72	13.88
225	4664	12 57 47.3	27 49 59	6041	32	19.1	16.25	14.39
226	5100	12 57 4.2	27 43 48	8884	36	9.9	17.34	15.63
227	4945	12 57 21.7	27 52 49	7427	32	18.7	16.72	15.00

Table 1—Continued

Fiber number	GMP83 number	RA ^a (J2000)	DEC ^a (J2000)	cz km/s	δcz km/s	R	b	r
228	4679	12 57 46.2	27 45 25	6133	32	18.0	16.11	14.17
229	4987	12 57 16.8	27 37 06	7238	32	18.7	16.86	14.97
231	4974	12 57 17.8	27 48 39	7136	33	15.7	16.59	14.98
232	5096	12 57 4.6	27 46 22	7577	36	9.0	17.00	15.17
234	5290	12 56 43.2	26 44 30	6950	33	15.2	17.44	15.56
236	5365	12 56 34.6	27 13 38	7197	39	8.5	16.60	14.87
237	5136	12 57 1.7	27 22 19	6979	32	19.9	16.66	14.70
238	5514	12 56 20.5	26 42 14	6558	33	15.0	17.39	15.54
240	5395	12 56 32.0	27 03 19	6105	32	18.5	16.19	14.33
241	5226	12 56 51.2	26 53 56	6247	32	19.9	15.42	13.68
242	5424	12 56 29.1	26 57 25	7035	32	19.8	15.20	13.32
243	5526	12 56 16.7	27 26 45	6386	31	20.6	16.50	14.56
244	5422	12 56 28.5	27 17 29	7526	33	10.7	15.74	14.18
246	5234	12 56 49.7	27 05 37	6934	33	14.3	15.89	13.87
247	5250	12 56 47.8	27 25 15	7758	32	17.2	17.12	15.29
248	5279	12 56 43.5	27 10 43	7607	33	18.4	14.00	11.98
249	5283	12 56 43.5	27 02 04	5586	32	18.1	16.88	15.03
250	5038	12 57 10.8	27 24 17	6193	33	13.0	16.25	14.33
251	5254	12 56 47.4	27 17 32	7854	36	9.4	17.86	16.15
252	5032	12 57 12.0	27 06 11	7333	34	11.2	17.66	15.78
253	5102	12 57 4.3	27 31 33	8296	33	13.0	17.66	15.70
254	5495	12 56 19.8	27 45 03	6859	32	19.7	15.80	13.87
255	5912	12 55 35.7	27 46 01	6680	33	14.4	17.17	15.29
256	5546	12 56 14.6	27 30 22	7422	32	18.3	17.51	15.60
257	5850	12 55 44.3	27 42 59	7138	32	14.7	18.03	16.06
258	5599	12 56 9.9	27 50 39	7566	31	21.9	15.96	13.95
259	5643	12 56 6.1	27 40 40	4909	31	21.3	16.00	14.51
260	5362	12 56 34.2	27 41 14	6872	32	17.4	17.83	15.93
261	5428	12 56 26.6	27 49 50	6268	32	20.4	15.69	13.80
262	5434	12 56 26.3	27 43 38	6823	31	21.2	16.96	15.03
264	5926	12 55 34.1	27 50 30	6997	31	20.6	16.94	15.00
266	5568	12 56 13.4	27 45 00	6817	91	2.9	15.19	13.66
267	5721	12 55 57.5	27 54 17	6551	32	14.9	17.44	15.48
268	5364	12 56 34.2	27 32 20	7086	32	20.1	16.03	14.07

Table 1—Continued

Fiber number	GMP83 number	RA ^a (J2000)	DEC ^a (J2000)	cz km/s	δcz km/s	R	b	r
271	5641	12 56 6.5	27 38 52	7593	32	19.9	16.74	14.88
272	5799	12 55 49.0	27 54 21	6930	31	21.4	16.49	14.57
273	6545	12 54 16.0	27 18 13	6422	32	20.1	15.32	13.32
275	6617	12 54 5.5	27 04 07	7589	32	18.9	15.41	13.46
279	6409	12 54 36.8	26 56 05	5913	32	16.5	15.59	13.75
280	5704	12 56 1.7	26 45 23	5722	33	15.3	16.57	14.67
282	6703	12 53 45.5	27 14 58	6902	35	11.4	17.73	15.88
285	6690	12 53 46.6	27 23 09	8317	43	5.0	17.84	15.92
287	6503	12 54 22.2	27 05 02	8427	32	21.1	16.51	14.52
289	5886	12 55 41.3	27 15 02	7105	33	17.8	15.05	13.06
291	5676	12 56 4.0	27 09 01	7337	33	15.8	17.97	16.05
292	6474	12 54 24.7	27 21 50	7833	39	8.6	17.55	15.64
293	6219	12 55 0.8	27 29 00	6968	36	7.9	17.34	15.51
294	6421	12 54 33.2	27 37 58	7265	33	13.8	15.96	13.91
295	6043	12 55 20.0	27 51 59	6978	32	16.3	16.33	14.46
296	5975	12 55 29.1	27 31 17	6983	32	21.5	14.36	12.49
297	6390	12 54 37.4	27 41 31	8453	32	19.1	17.66	15.79
302	-	12 53 37.9	27 47 03	5088	32	18.2	15.80	13.89
303	5999	12 55 25.0	27 47 53	7382	32	19.7	15.20	12.93
304	6109	12 55 13.9	27 42 32	6647	32	15.1	17.70	15.76
306	-	12 53 30.3	27 40 30	5919	31	20.8	17.50	15.59
307	5960	12 55 30.6	27 32 39	7024	32	14.8	16.76	14.80
308	6701	12 53 44.1	27 46 51	6640	32	16.5	17.81	15.96
309	6479	12 54 22.7	27 44 40	7102	36	9.5	18.04	16.27
311	-	12 53 35.5	27 45 31	7463	33	14.4	16.95	15.08
312	5978	12 55 27.8	27 39 22	6997	32	18.8	15.33	13.36

^aPosition of the fiber. For some objects this is a bit off of the galaxy.

Table 2. Galaxy Classifications.

Fiber number	Line Strengths	PCA	Wavelet	Spectral_1			Spectral_2			Principal Component Analysis coefficients					
				age (Gyr)	SF	χ^2/ν	age (Gyr)	τ (Gyr)	χ^2/ν	c_1	c_2	c_3	θ	ϕ	radius ²
3	AB	AB	AB	5.00	1	0.78	4.44	0.011	0.78	0.781	-0.069	0.128	9.30	-5.03	0.632
4	AB	AB	AB	6.14	2	0.51	4.20	0.607	0.51	0.846	-0.071	0.109	7.33	-4.80	0.733
10	AB	AB	AB	17.00	3	0.55	15.25	2.718	0.58	0.970	-0.112	-0.023	-1.35	-6.58	0.954
11	AB	AB	AB	13.79	1	2.68	18.86	2.718	2.45	0.948	-0.181	-0.178	-10.48	-10.79	0.962
12	EM+AB	EM	EM	2.26	3	0.79	1.21	0.368	0.93	0.335	0.843	-0.219	-13.53	68.31	0.871
13	AB	AB+EM	AB	1.98	1	0.91	1.20	0.002	0.90	0.534	0.243	0.239	22.16	24.52	0.401
14	AB	AB	AB	18.76	5	0.61	9.00	1.649	0.72	0.974	-0.044	0.046	2.72	-2.60	0.953
21	AB	AB	AB	17.04	2	2.52	16.63	2.718	2.62	0.957	-0.127	-0.040	-2.39	-7.55	0.935
27	AB	AB	AB	19.00	4	0.96	10.35	1.649	1.08	0.979	-0.022	0.062	3.64	-1.26	0.962
28	AB	AB	AB	19.00	4	0.47	10.44	1.649	0.52	0.946	0.079	0.175	10.47	4.77	0.931
29	AB	AB	AB	17.79	4	0.44	9.84	1.649	0.51	0.915	0.008	0.072	4.51	0.52	0.843
30	AB	AB	AB	16.26	5	0.17	3.95	0.607	0.18	0.662	0.200	0.286	22.49	16.82	0.561
31	EM+AB	EM	EM	3.04	3	7.99	1.49	0.368	8.84	0.478	0.796	-0.097	-5.97	59.01	0.872
32	AB	AB	AB	19.00	4	0.74	14.98	2.718	0.82	0.988	-0.041	0.025	1.44	-2.40	0.979
34	AB+EM	AB+EM	EM	17.88	5	2.28	19.00	4.482	2.69	0.786	0.288	-0.259	-17.16	20.12	0.768
40	AB	AB	AB	16.98	5	0.42	4.05	0.607	0.48	0.758	-0.023	0.091	6.87	-1.75	0.584
43	AB	AB	AB	17.16	4	0.62	9.60	1.649	0.73	0.958	0.023	0.145	8.60	1.36	0.939
45	PS	PS	PS	1.26	1	0.37	0.60	0.018	0.39	0.483	0.484	0.587	40.61	45.06	0.813
50	AB	AB	AB	19.00	2	2.47	18.18	2.718	2.36	0.987	-0.116	-0.008	-0.47	-6.73	0.988
55	AB	AB	AB	13.46	2	0.89	11.02	1.649	0.94	0.984	-0.067	0.005	0.31	-3.91	0.973
58	PS	PS	PS	1.46	2	4.11	1.21	0.223	3.70	0.696	0.518	0.374	23.32	36.69	0.892
61	AB	AB	AB	19.00	5	0.65	13.58	2.718	0.78	0.929	0.087	0.195	11.78	5.37	0.908
65	AB	AB	AB	19.00	4	1.10	14.99	2.718	1.21	0.978	-0.036	0.068	3.96	-2.11	0.962
66	AB	AB	AB	18.61	4	0.85	9.97	1.649	0.96	0.984	-0.046	0.062	3.59	-2.65	0.974
68	AB	AB	AB	9.82	2	0.60	6.93	1.000	0.62	0.976	0.024	0.087	5.10	1.41	0.960
69	AB	AB	AB	18.27	2	2.63	17.07	2.718	2.67	0.971	-0.134	-0.083	-4.83	-7.86	0.968
70	AB	AB	AB	14.57	2	1.67	11.46	1.649	1.70	0.978	-0.117	-0.017	-1.00	-6.82	0.971
74	AB	AB	AB	19.00	1	3.75	19.00	0.011	3.73	0.841	-0.100	0.015	1.01	-6.76	0.717
75	AB	AB	AB	18.00	1	15.71	19.00	0.002	15.19	0.954	-0.122	-0.056	-3.34	-7.29	0.928
76	AB	AB	AB	13.00	1	3.19	14.60	1.649	3.18	0.844	-0.008	0.177	11.87	-0.56	0.743
84	EM+AB	EM	AB	3.98	4	0.29	2.09	0.607	0.36	0.388	0.788	-0.240	-15.26	63.79	0.829
85	AB+EM	AB+EM	AB	18.41	2	2.65	16.68	2.718	2.72	0.805	0.409	-0.060	-3.78	26.92	0.819
86	AB	AB	AB	19.00	3	0.98	16.14	2.718	1.05	0.981	-0.066	0.035	2.06	-3.84	0.967
87	AB	AB	AB	17.07	1	0.48	16.86	0.368	0.47	0.934	-0.058	0.049	3.02	-3.57	0.878
88	AB	AB	AB	13.83	1	2.25	18.94	2.718	2.10	0.971	-0.143	-0.089	-5.20	-8.40	0.972
89	AB	AB	AB	17.58	2	0.70	16.91	2.718	0.73	0.967	0.004	0.128	7.54	0.22	0.952
91	AB+EM	PS	PS	1.98	1	1.23	1.20	0.002	1.20	0.755	0.463	0.420	25.39	31.52	0.961
94	AB	AB	AB	17.53	1	2.41	16.74	0.011	2.33	0.950	-0.204	-0.165	-9.64	-12.14	0.970
95	PS	PS	PS	1.39	1	1.79	0.85	0.082	1.92	0.544	0.528	0.564	36.65	44.12	0.893
96	AB	AB	AB	16.00	1	1.12	17.25	1.649	1.09	0.969	-0.166	-0.121	-7.02	-9.73	0.981
97	AB	AB	AB	19.00	2	0.83	17.57	2.718	0.86	0.983	-0.109	-0.053	-3.05	-6.35	0.982
98	EM+AB	EM	EM	1.96	3	4.15	0.86	0.223	4.62	0.328	0.851	-0.178	-11.06	68.94	0.864
99	AB	AB	AB	15.49	1	1.50	16.80	1.649	1.45	0.962	-0.187	-0.131	-7.59	-10.99	0.977
100	AB	AB	AB	18.22	2	0.52	17.21	2.718	0.53	0.962	0.029	0.071	4.20	1.70	0.931
101	AB	AB+EM	AB	19.00	1	0.20	19.00	0.007	0.19	0.435	0.164	0.192	22.41	20.69	0.253
102	AB	AB	PS	15.67	4	0.63	3.49	0.368	0.66	0.909	0.169	0.292	17.52	10.56	0.941
103	AB	AB	AB	16.17	2	1.03	16.38	2.718	1.09	0.982	-0.078	-0.032	-1.86	-4.56	0.971
105	AB	AB	AB	17.35	3	0.69	15.44	2.718	0.73	0.902	-0.107	-0.068	-4.30	-6.79	0.830
106	AB+EM	AB+EM	AB	18.09	5	2.06	13.15	2.718	2.52	0.791	0.342	0.009	0.62	23.40	0.743
107	AB	AB	AB	16.50	2	0.87	16.51	2.718	0.89	0.937	-0.071	-0.043	-2.61	-4.31	0.886
108	AB	AB	AB	14.27	4	1.12	4.11	0.607	1.15	0.964	-0.029	-0.004	-0.24	-1.73	0.930
110	EM+AB	EM	EM	2.56	3	2.54	1.33	0.368	2.95	0.260	0.751	-0.465	-30.31	70.92	0.848
111	AB	AB	AB	17.33	2	0.50	16.82	2.718	0.51	0.934	-0.002	0.034	2.07	-0.14	0.874
115	EM	EM	EM	0.02	5	6.54	0.06	90.017	6.04	-0.086	0.534	-0.529	-44.34	80.80	0.572
117	EM+AB	EM	EM	4.62	4	3.05	1.58	0.368	3.60	0.449	0.849	-0.093	-5.54	62.11	0.932
120	AB	AB	AB	17.58	1	4.64	18.69	1.649	4.50	0.947	-0.160	-0.145	-8.57	-9.59	0.942
123	AB	AB	AB	10.33	2	1.47	7.10	1.000	1.57	0.977	-0.143	-0.062	-3.59	-8.33	0.978
124	AB	AB	AB	4.01	1	0.96	3.48	0.135	0.95	0.979	-0.069	0.022	1.31	-4.01	0.964
126	EM	EM	EM	2.57	6	5.02	1.40	0.607	6.12	0.146	0.810	-0.467	-29.58	79.78	0.895
127	EM	EM	EM	12.66	7	2.13	14.78	7.389	1.97	0.142	0.778	-0.552	-34.91	79.63	0.930
130	AB	AB	AB	13.61	2	1.45	11.06	1.649	1.45	0.985	-0.080	0.019	1.09	-4.62	0.976
131	AB+EM	AB+EM	PS	11.54	5	0.54	2.39	0.368	0.60	0.739	0.459	0.144	9.36	31.83	0.778
132	AB+EM	AB+EM	AB	15.82	6	0.67	2.37	0.368	0.74	0.645	0.268	-0.080	-6.52	22.56	0.494
133	AB	AB	AB	19.00	3	0.54	16.03	2.718	0.56	0.965	-0.067	-0.031	-1.80	-3.97	0.938
134	AB	AB	AB	13.68	2	0.33	11.21	1.649	0.33	0.915	-0.015	0.025	1.55	-0.92	0.837
135	AB	AB	AB	18.21	2	2.06	17.06	2.718	2.12	0.969	-0.110	-0.061	-3.58	-6.48	0.955
136	AB	AB	AB	14.25	1	1.87	19.00	2.718	1.77	0.970	-0.101	0.015	0.87	-5.95	0.951
137	AB	AB	AB	17.83	2	3.63	12.66	1.649	3.72	0.935	-0.173	-0.163	-9.75	-10.46	0.932
138	EM+AB	EM	AB	0.97	2	2.10	0.94	0.223	2.30	0.437	0.782	-0.146	-9.26	60.78	0.824
139	AB	AB	AB	18.83	2	1.75	13.21	1.649	1.72	0.978	-0.111	0.013	0.76	-6.45	0.970

Table 2—Continued

Fiber number	Line Strengths	PCA	Wavelet	Spectral ₁			Spectral ₂			Principal Component Analysis coefficients						
				age (Gyr)	SF	χ^2/ν	age (Gyr)	τ (Gyr)	χ^2/ν	c_1	c_2	c_3	θ	ϕ	radius ²	
140	AB+EM	PS	PS	1.22	1	1.22	0.76	0.135	1.24	0.511	0.570	0.492	32.75	48.10	0.828	
141	AB+EM	AB	AB	18.80	3	0.73	15.82	2.718	0.75	0.964	0.019	0.059	3.51	1.13	0.932	
142	AB	AB	AB	15.10	1	2.88	16.47	1.649	2.80	0.945	-0.179	-0.180	-10.59	-10.72	0.958	
143	AB	AB	AB	16.00	2	2.19	16.31	2.718	2.29	0.986	-0.108	-0.072	-4.14	-6.24	0.989	
144	AB	AB	AB	19.00	1	0.46	18.95	0.050	0.45	0.932	-0.121	-0.105	-6.35	-7.39	0.893	
145	AB	AB	AB	13.52	2	0.98	11.10	1.649	0.99	0.979	-0.094	-0.005	-0.29	-5.51	0.967	
146	AB	AB	AB	19.00	5	0.37	6.48	1.000	0.40	0.820	0.157	0.209	14.07	10.82	0.740	
147	AB	AB	AB	12.31	1	1.71	14.15	1.649	1.66	0.960	-0.187	-0.160	-9.29	-11.01	0.983	
148	AB	AB	AB	14.14	2	1.03	11.34	1.649	1.05	0.965	-0.111	-0.054	-3.17	-6.58	0.947	
149	AB	AB	AB	14.14	2	1.12	11.31	1.649	1.12	0.984	-0.026	0.032	1.84	-1.52	0.971	
150	AB	AB	AB	19.00	1	0.86	19.00	0.002	0.82	0.695	-0.125	-0.042	-3.44	-10.21	0.500	
151	AB	AB	AB	8.80	1	0.52	8.66	0.607	0.52	0.951	-0.095	-0.022	-1.32	-5.69	0.914	
152	AB	AB	AB	14.02	1	0.59	15.58	1.649	0.58	0.962	0.019	0.061	3.62	1.15	0.930	
153	AB	AB	AB	14.09	1	3.07	19.00	2.718	2.87	0.957	-0.159	-0.143	-8.37	-9.45	0.962	
155	AB	AB	AB	15.35	4	0.29	4.42	0.607	0.31	0.808	-0.021	0.091	6.46	-1.46	0.661	
156	AB	AB	AB	17.50	5	0.57	5.90	1.000	0.62	0.851	0.054	0.161	10.67	3.66	0.753	
158	AB	AB	AB	19.00	2	0.51	18.16	2.718	0.50	0.960	-0.132	-0.113	-6.63	-7.80	0.951	
160	AB	AB	AB	16.05	2	1.99	11.95	1.649	1.98	0.952	-0.184	-0.150	-8.79	-10.96	0.964	
161	AB	AB	AB	16.49	2	1.54	16.50	2.718	1.61	0.984	-0.118	-0.070	-4.05	-6.82	0.987	
162	AB	AB	AB	14.30	2	1.44	11.38	1.649	1.44	0.957	-0.173	-0.155	-9.05	-10.26	0.970	
163	AB	AB	AB	17.89	2	1.71	12.69	1.649	1.70	0.963	-0.173	-0.159	-9.25	-10.19	0.982	
164	AB	AB	AB	17.18	2	2.90	12.41	1.649	2.83	0.961	-0.161	-0.160	-9.34	-9.51	0.976	
165	AB	AB	AB	19.00	2	2.01	17.71	2.718	1.99	0.943	-0.156	-0.101	-6.06	-9.41	0.923	
166	AB	AB	AB	13.89	2	1.02	11.22	1.649	1.02	0.982	-0.134	-0.089	-5.11	-7.78	0.990	
167	AB	AB	AB	12.87	1	0.70	18.43	2.718	0.68	0.938	-0.147	-0.105	-6.28	-8.90	0.913	
168	EM+AB	EM	EM	1.15	1	10.68	0.86	0.223	12.70	0.205	0.632	-0.356	-28.16	72.04	0.567	
169	AB+EM	AB	AB	18.31	2	2.44	17.08	2.718	2.54	0.945	-0.173	-0.175	-10.33	-10.38	0.954	
172	AB+EM	AB+EM	AB	17.24	5	1.78	5.81	1.000	2.34	0.965	0.199	0.123	7.10	11.65	0.986	
173	AB	AB	AB	19.00	2	1.59	17.96	2.718	1.55	0.983	-0.092	-0.019	-1.10	-5.34	0.974	
174	AB	AB	AB	17.48	2	0.68	12.69	1.649	0.69	0.961	-0.039	-0.004	-0.25	-2.33	0.926	
175	AB	AB	AB	16.49	2	0.92	16.54	2.718	0.92	0.949	-0.012	-0.023	-1.41	-0.71	0.902	
178	EM+AB	EM	EM	2.00	4	1.64	1.08	0.368	2.02	0.194	0.791	-0.472	-30.10	76.19	0.887	
179	AB	AB	AB	14.41	2	1.60	15.74	2.718	1.64	0.980	-0.084	-0.071	-4.12	-4.89	0.972	
180	AB+EM	AB+EM	PS	12.64	5	2.61	3.33	0.607	3.02	0.801	0.465	0.208	12.64	30.14	0.902	
181	AB	AB	AB	17.33	4	0.55	13.91	2.718	0.61	0.872	0.119	0.066	4.28	7.77	0.779	
182	AB+EM	AB+EM	PS	14.38	5	12.00	3.51	0.607	14.82	0.921	0.283	0.173	10.16	17.06	0.957	
183	PS	PS	PS	1.01	2	0.67	0.77	0.135	0.69	0.378	0.462	0.536	41.90	50.70	0.644	
184	PS	PS	PS	1.29	1	0.68	0.83	0.135	0.70	0.482	0.592	0.527	34.60	50.84	0.861	
185	AB	AB	AB	15.20	2	1.57	11.68	1.649	1.57	0.962	-0.133	-0.107	-6.28	-7.89	0.956	
187	AB	AB	AB	4.55	2	0.51	3.81	0.607	0.51	0.772	-0.024	-0.067	-4.98	-1.78	0.602	
190	AB	AB	AB	5.06	2	0.79	3.93	0.607	0.77	0.938	-0.015	-0.019	-1.16	-0.93	0.880	
191	AB	AB	AB	19.00	2	2.23	17.46	2.718	2.18	0.973	-0.127	-0.097	-5.63	-7.44	0.971	
192	AB	AB	AB	13.14	2	0.69	10.92	1.649	0.71	0.946	0.036	0.013	0.81	2.21	0.897	
193	AB	AB	AB	3.53	1	1.57	4.35	0.607	1.54	0.981	-0.070	-0.001	-0.08	-4.07	0.967	
194	AB	AB	AB	18.06	2	1.90	16.94	2.718	1.96	0.975	-0.103	-0.093	-5.44	-6.02	0.969	
196	AB+EM	AB+EM	AB	15.53	5	1.92	5.48	1.000	2.56	0.949	0.161	0.061	3.63	9.60	0.930	
197	AB	AB	AB	14.26	2	3.11	11.34	1.649	3.11	0.960	-0.084	0.031	1.82	-5.02	0.929	
201	EM+AB	EM	AB	3.05	3	0.83	1.47	0.368	0.94	0.522	0.776	-0.128	-7.81	56.06	0.892	
202	AB+EM	AB+EM	AB	17.17	3	0.81	15.31	2.718	0.83	0.867	0.222	0.168	10.63	14.38	0.829	
204	AB	AB	AB	3.41	2	0.67	2.69	0.368	0.68	0.867	0.181	0.300	18.71	11.77	0.875	
205	AB	AB	AB	18.35	4	0.68	9.96	1.649	0.71	0.874	-0.063	-0.029	-1.89	-4.13	0.769	
209	EM+AB	EM	EM	13.15	8	2.82	3.26	1.000	3.08	0.542	0.516	-0.569	-37.26	43.58	0.884	
210	AB	AB	AB	16.90	3	0.81	15.19	2.718	0.85	0.969	0.028	0.037	2.21	1.65	0.941	
212	AB	AB	AB	3.59	2	0.30	2.76	0.368	0.31	0.907	0.114	0.233	14.31	7.16	0.890	
213	AB	AB	AB	14.85	1	0.43	19.00	2.718	0.41	0.918	-0.043	-0.106	-6.57	-2.66	0.855	
216	AB	AB	AB	10.86	2	0.71	10.13	1.649	0.74	0.980	-0.014	0.002	0.09	-0.84	0.961	
218	AB	AB	AB	18.14	1	5.03	19.00	1.649	4.92	0.923	-0.222	-0.226	-13.38	-13.53	0.951	
219	AB+EM	AB	AB	15.40	1	3.41	19.00	2.718	3.30	0.955	-0.153	-0.148	-8.72	-9.10	0.957	
220	AB	AB	AB	18.74	2	2.28	13.08	1.649	2.20	0.955	-0.184	-0.168	-9.80	-10.89	0.973	
221	AB	AB	AB	19.00	2	2.75	13.26	1.649	2.69	0.965	-0.146	-0.105	-6.16	-8.63	0.963	
222	AB+EM	AB+EM	AB	9.99	4	0.72	2.49	0.368	0.78	0.882	0.221	-0.071	-4.47	14.07	0.832	
223	AB	AB	AB	13.21	3	0.74	9.70	1.649	0.80	0.957	-0.069	0.038	2.29	-4.12	0.922	
224	AB	AB	AB	16.00	2	1.64	11.90	1.649	1.63	0.966	-0.159	-0.143	-8.32	-9.33	0.980	
225	AB	AB	AB	13.43	2	1.97	10.98	1.649	1.91	0.978	-0.128	-0.099	-5.75	-7.47	0.982	
226	AB+EM	AB+EM	AB	2.87	2	0.34	2.42	0.368	0.34	0.764	0.256	0.266	18.25	18.50	0.719	
227	AB	AB	PS	2.23	1	1.46	1.91	0.223	1.45	0.917	0.214	0.311	18.27	13.12	0.984	
228	AB	AB	AB	7.30	1	0.44	10.82	1.649	0.42	0.976	-0.063	-0.010	-0.56	-3.69	0.956	
229	AB	AB	AB	15.60	2	1.42	11.77	1.649	1.46	0.986	-0.090	-0.050	-2.90	-5.21	0.983	
231	AB	AB+EM	PS	1.82	1	0.85	1.18	0.082	0.82	0.845	0.318	0.378	22.73	20.63	0.959	
232	AB+EM	AB+EM	PS	18.77	6	0.81	3.42	0.607	1.08	0.854	0.403	0.065	3.97	25.25	0.895	

Table 3. Line Strengths versus PCA classification

PCA \ Line Strengths	AB	PS	AB+EM	EM+AB	EM	Total
AB	144	0	6	0	0	150
PS	0	5	2	0	0	7
AB+EM	3	0	19	0	0	22
EM	0	0	1	12	4	17
Total	147	5	28	12	4	196

Table 4. Line Strengths versus Wavelet classification

Wavelet \ Line Strengths	AB	PS	AB+EM	EM+AB	EM	Total
AB	144	0	19	4	0	167
PS	3	5	7	0	0	15
EM	0	0	2	8	4	14
Total	147	5	28	12	4	196

Table 5. PCA versus Wavelet classification schemes

Wavelet \ PCA	AB	PS	AB+EM	EM	Total
AB	148	0	15	4	167
PS	2	7	6	0	15
EM	0	0	1	13	14
Total	150	7	22	17	196

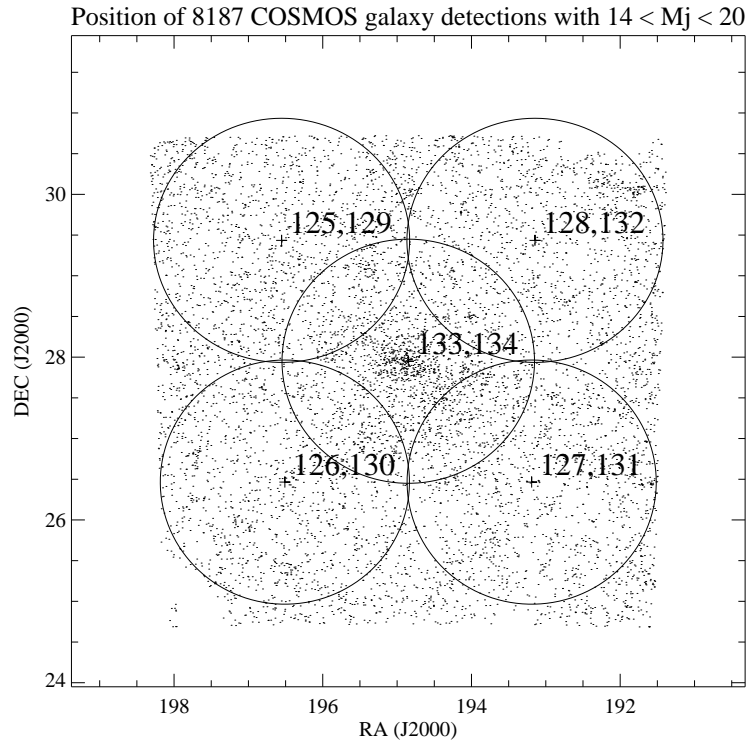


Fig. 1.— The distribution of SuperCOSMOS galaxies in the Coma cluster region. The circles superimposed on the data show the position of our 10 designed plug-plates. We designed two plates at each position: one containing the brighter sources, the other, fainter sources. The numbers are the SDSS plate identifiers.

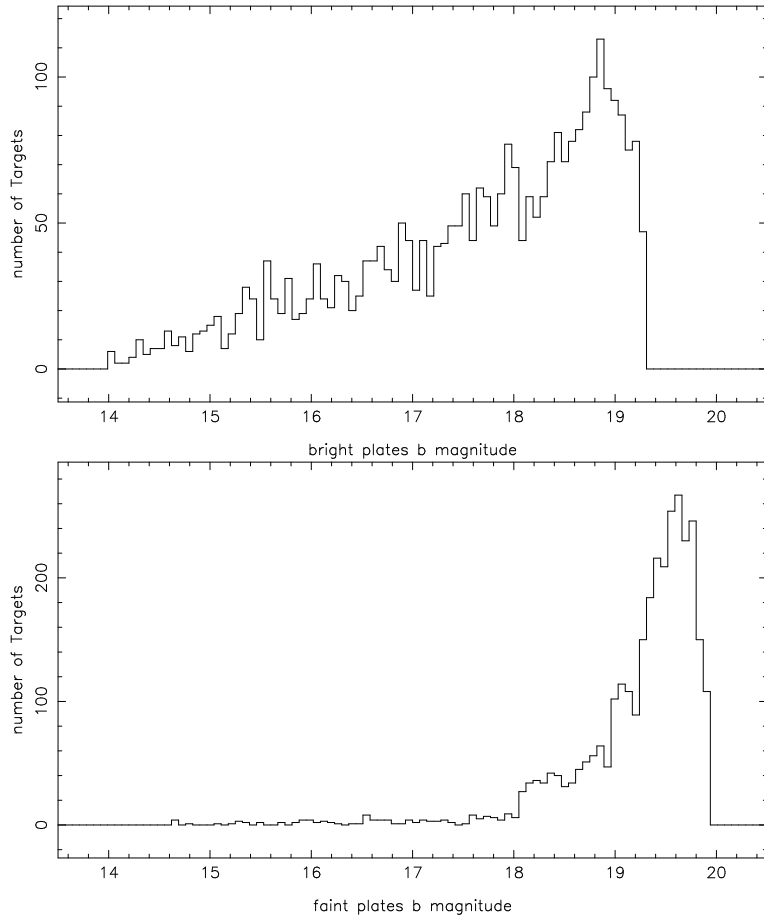


Fig. 2.— Magnitude distribution of selected sources in the five *bright* plates (top) and the five *faint* plates (bottom).

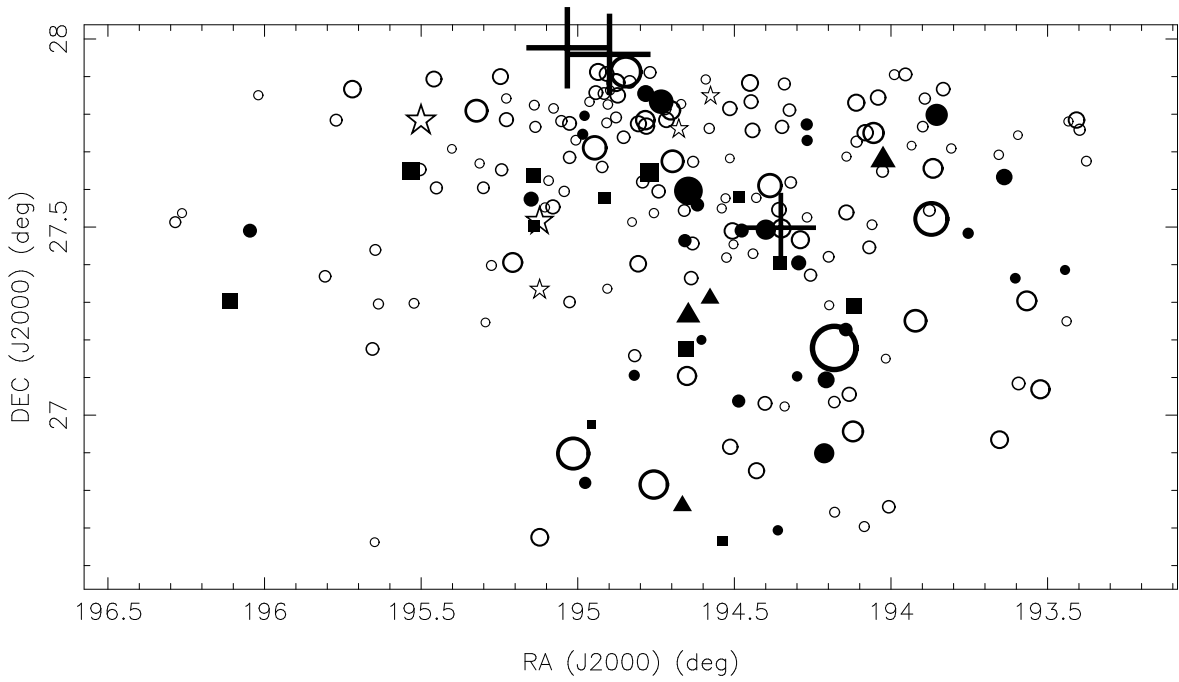


Fig. 3.— Distribution on the sky of the observed Coma galaxies. The different symbols represent different galaxy types: **AB** open circles; **AB+EM** solid circles; **EM+AB** solid squares; **EM** solid triangles; **PS** stars (see text). The position of NGC4874, NGC4889 and NGC4839 are also shown as plus signs. The size of the symbols denotes the b magnitude of the object, from the brightest (largest symbol) $b = 14.0$, to the faintest (smallest) $b = 18.0$, excluding the plus signs.

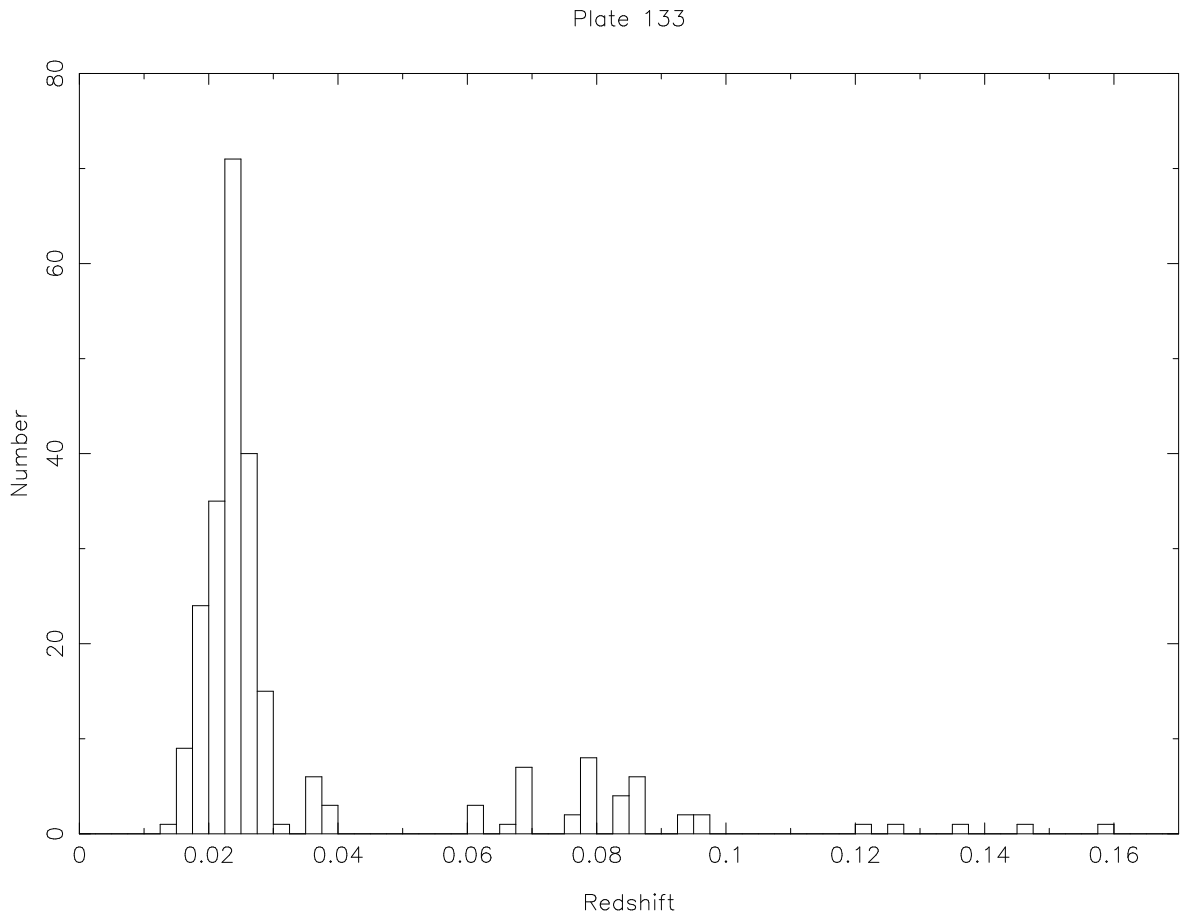


Fig. 4.— The redshift distribution of the all identified galaxies in plate 133.

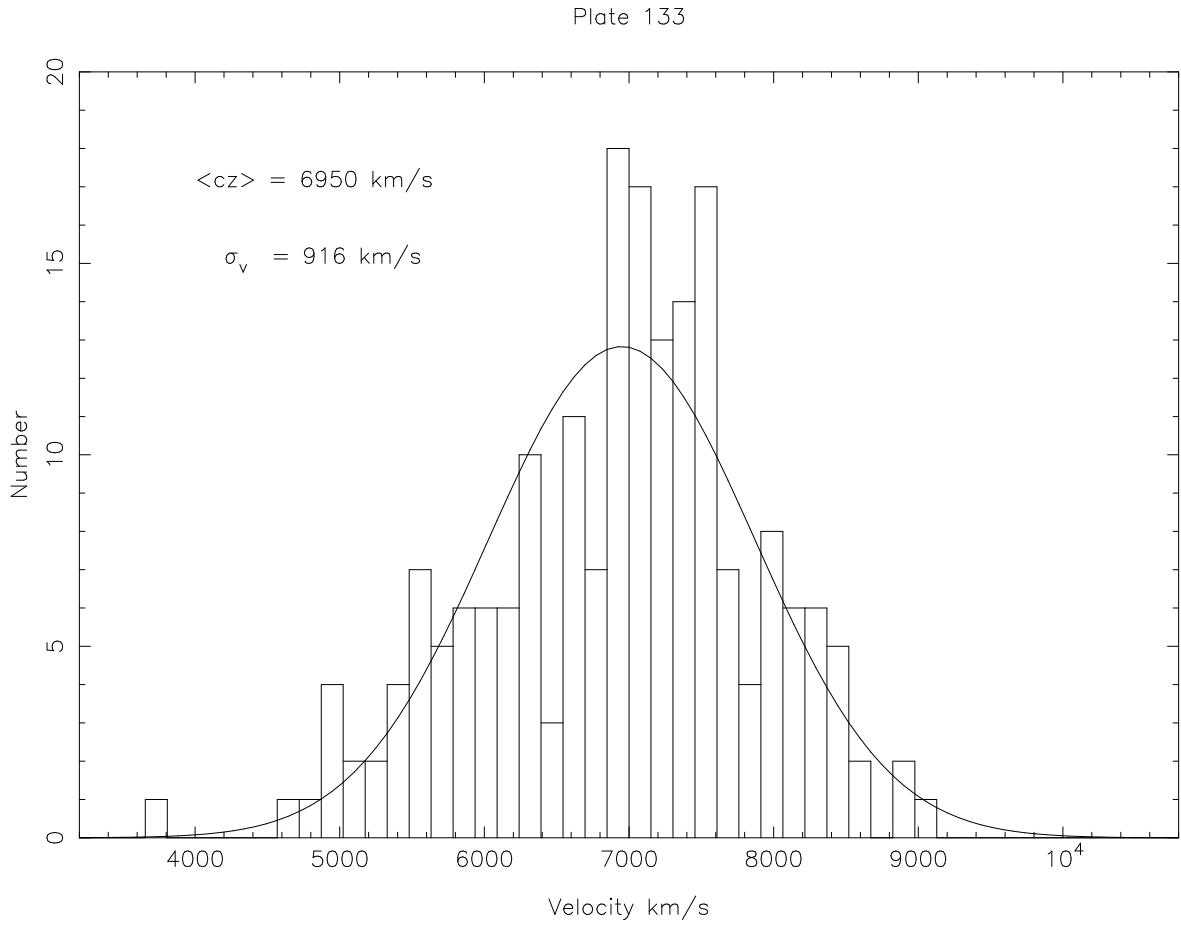


Fig. 5.— The redshift distribution of the Coma galaxies in plate 133.

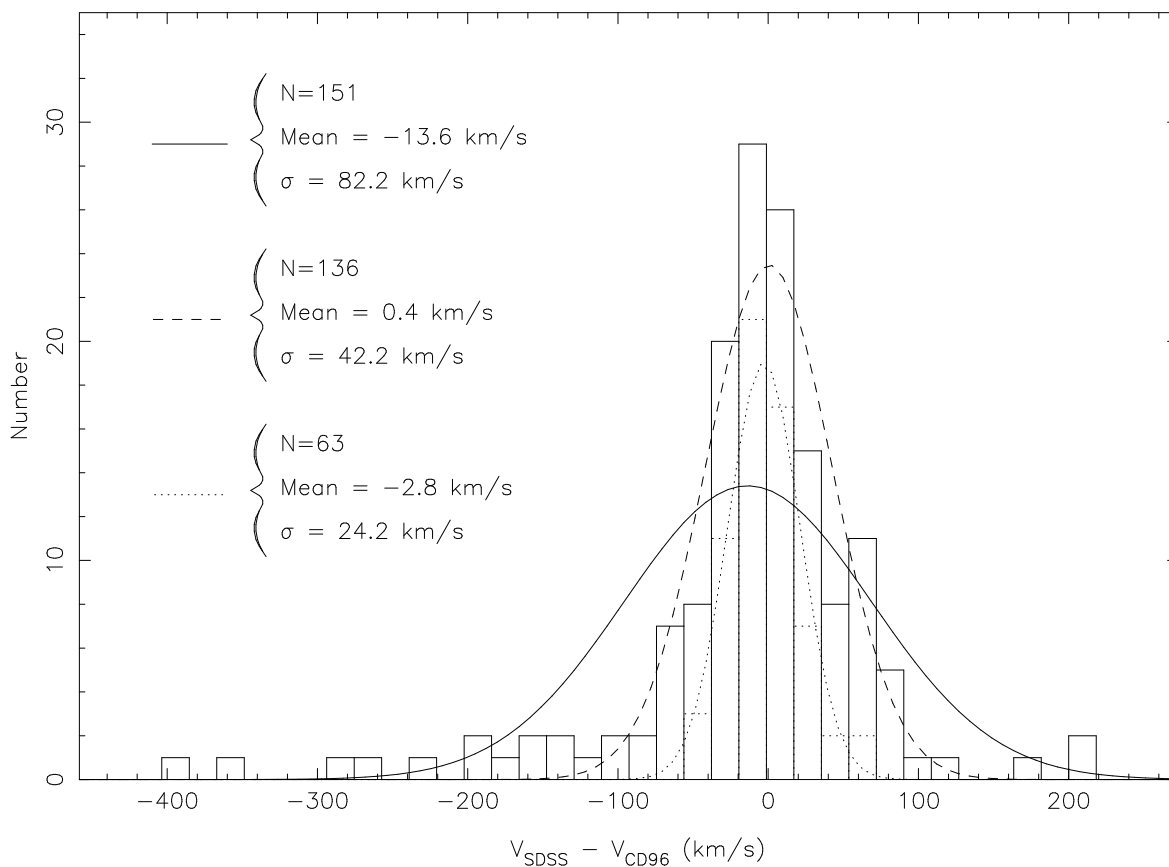


Fig. 6.— Distribution of the difference in cz between the our redshift measurements (Table 1) and those in the literature. The solid histogram represents all 151 matches. The solid line is a Gaussian fit to the whole histogram. The dash line is a Gaussian fit to the histogram with $3\text{-}\sigma$ clipping rejection. The dotted histogram counts only the galaxies that were measured by CD96 and not taken from the literature by these authors. The dotted histogram is a Gaussian fit to it. (See text for further details).

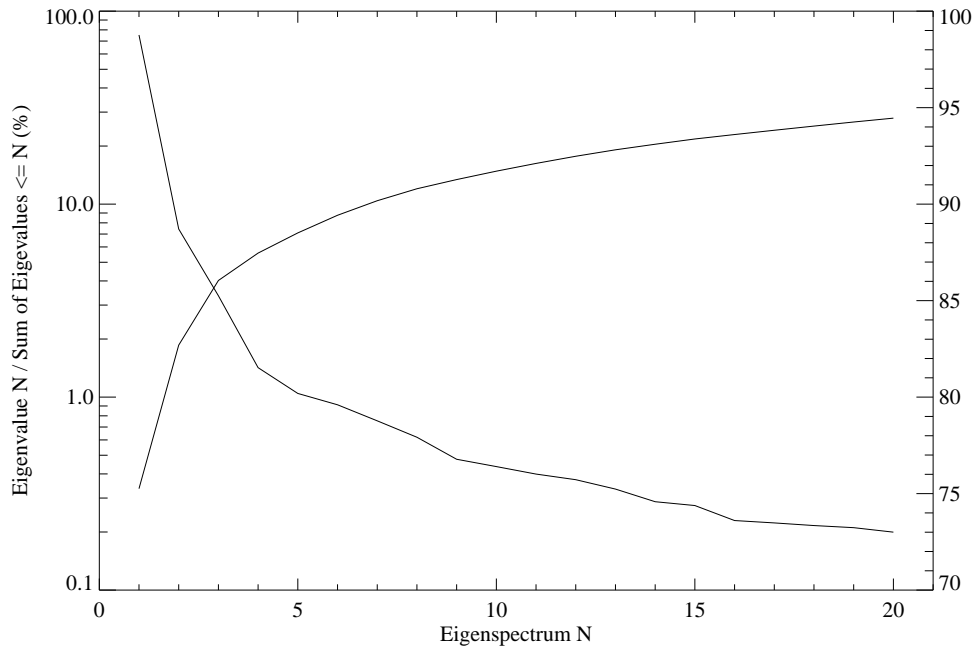


Fig. 7.— Distribution of the first 20 eigenvalues. The decreasing function is the percentage contribution of the Nth eigenvalue, and uses the left logarithmic axis. The increasing function is the cumulative percentage contribution by the first N eigenvalues, and uses the right linear axis.

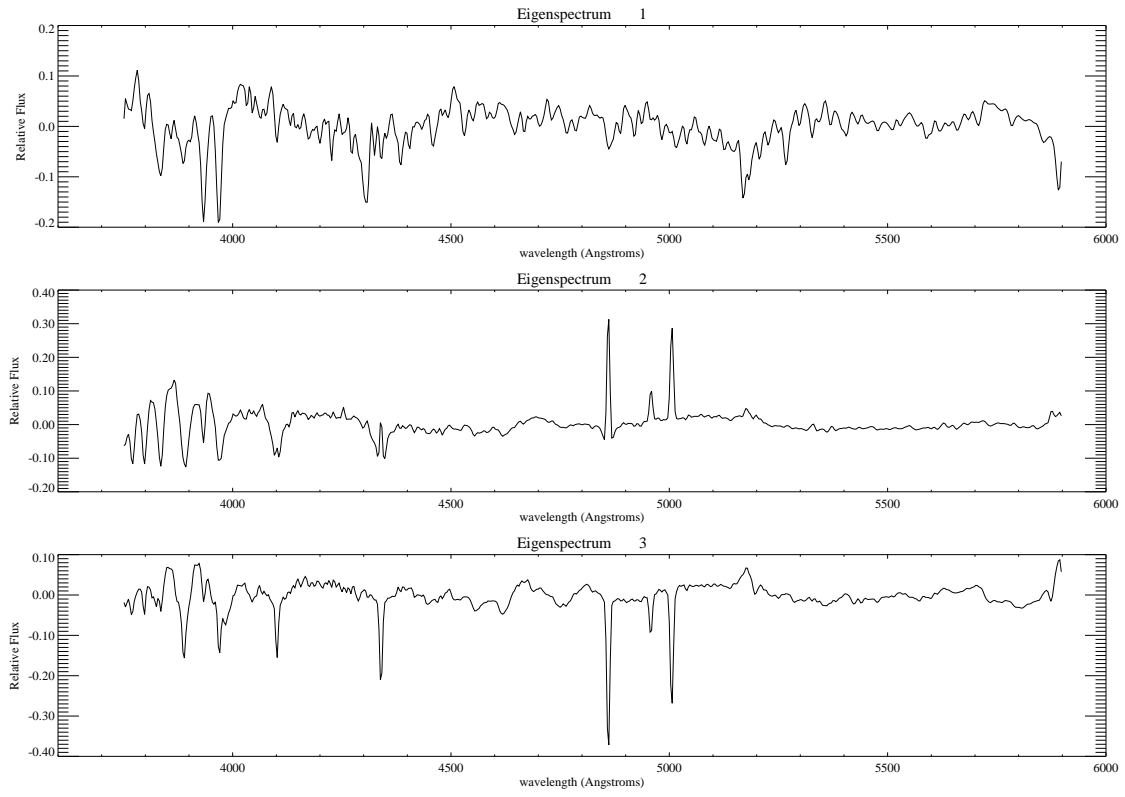


Fig. 8.— The first three Eigenspectra (see text)

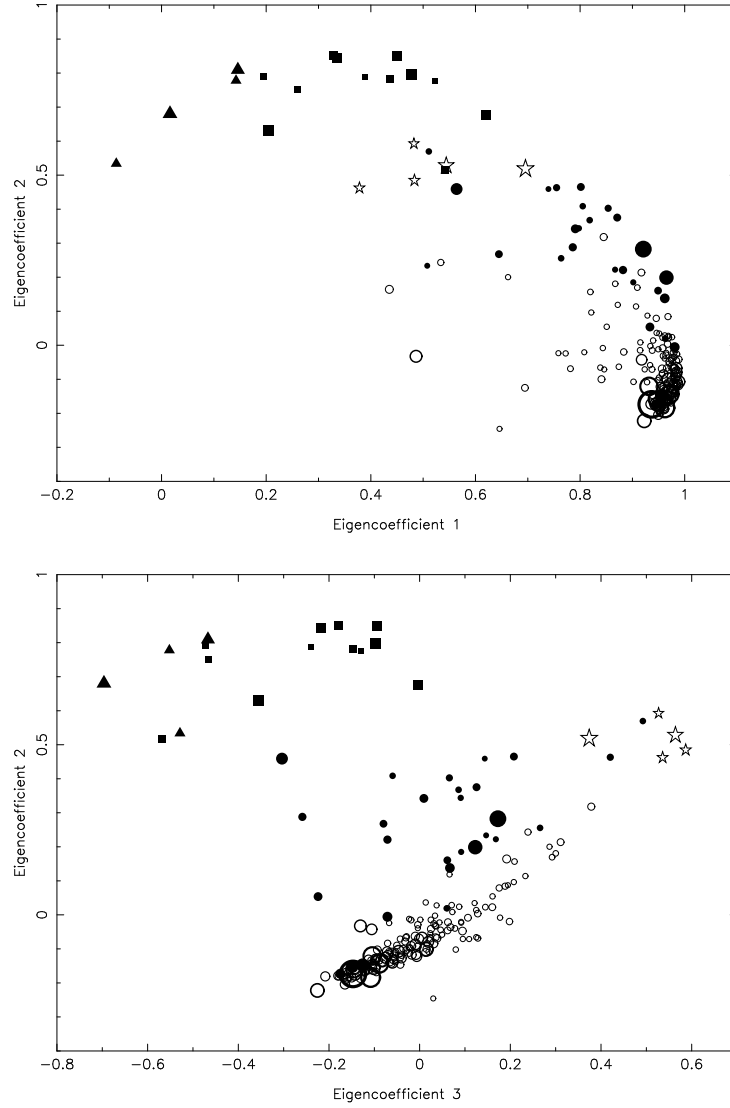


Fig. 9.— The first three eigencoefficients. The symbols are our line strength classification scheme; **AB** are open circles, **AB+EM** are solid circles, **EM+AB** are solid squares, **EM** are solid triangles and **PS** are stars. The size of the symbol is proportional to the magnitude of the galaxy as in Figure 3.

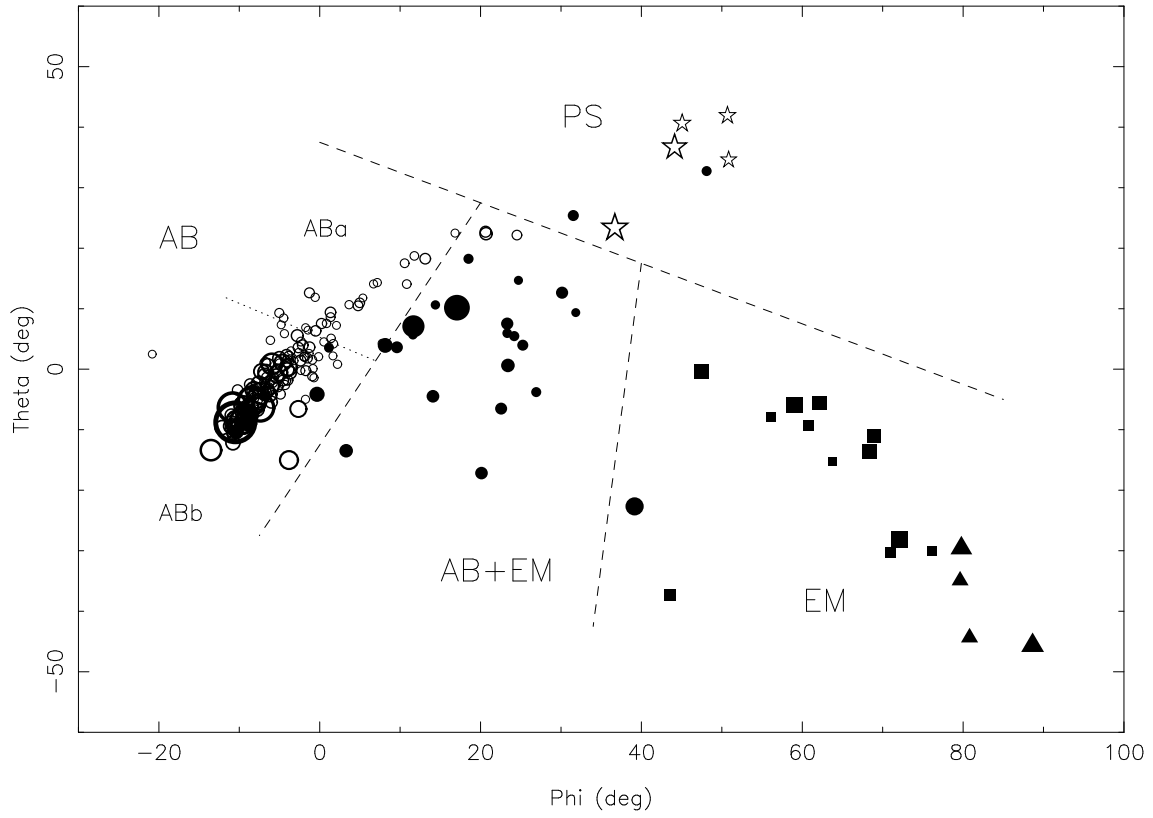


Fig. 10.— Plot of the spherical projection of the first three eigencoefficients. The plot symbols are the same as in Figure 3 and 9. We show the cuts in eigenspace we have used to objectively classify our spectra. For this scheme, we have merged the **EM** and **EM+AB** types into the one type (**EM**).

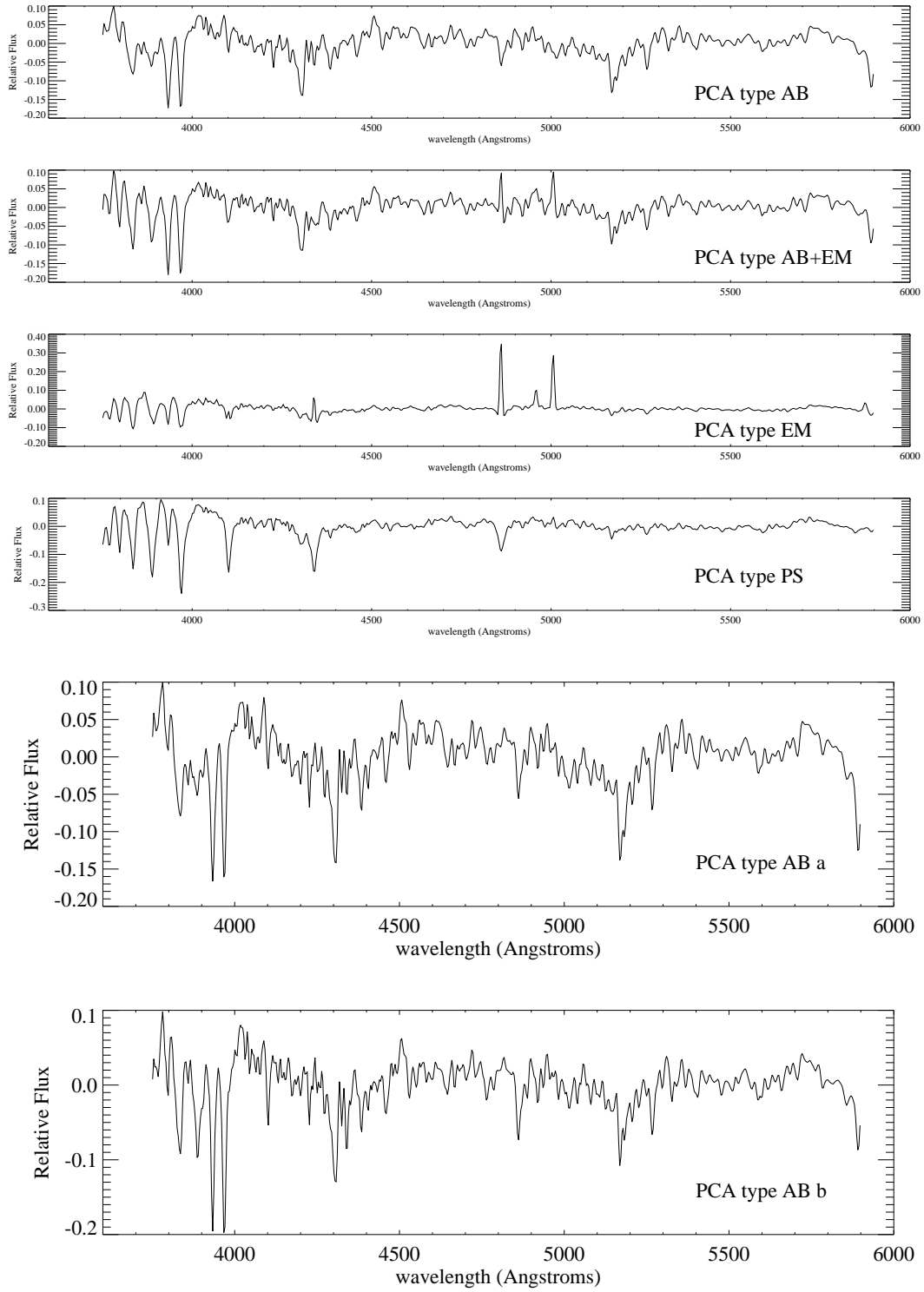


Fig. 11.— Composite spectra of the four PCA spectral types, and the two sub A types. The spectra for all the members of each group have been averaged with a uniform weight.

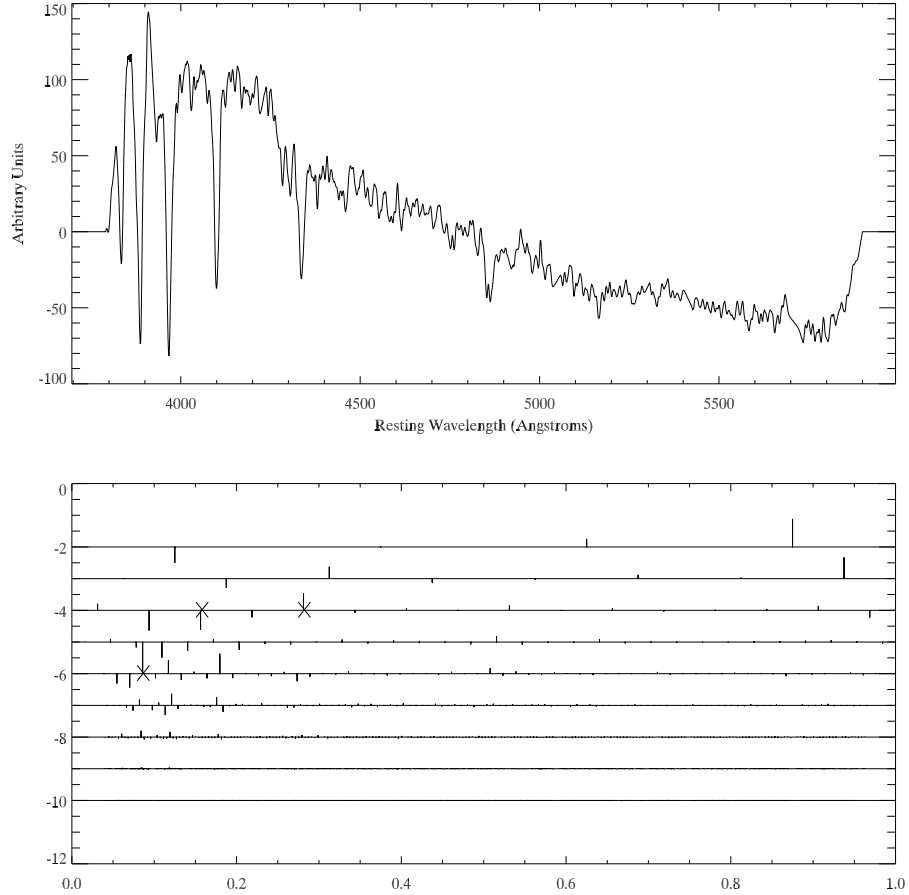


Fig. 12.— Top: The spectrum of one of the Coma post–starburst galaxies. We have subtracted off the mean pixel value as well as padded the ends with zeros to be 2048 pixels. Cosine–bell smoothing was applied to the ends to smoothly taper them to zero. Bottom: The different wavelet resolution levels start at the top with the lowest resolution and moving to higher resolutions towards the bottom of the figure. We show the relative height and sign of the wavelet coefficients. The crosses make the three wavelet coefficients used to classify this spectrum as a post–starburst (see text).

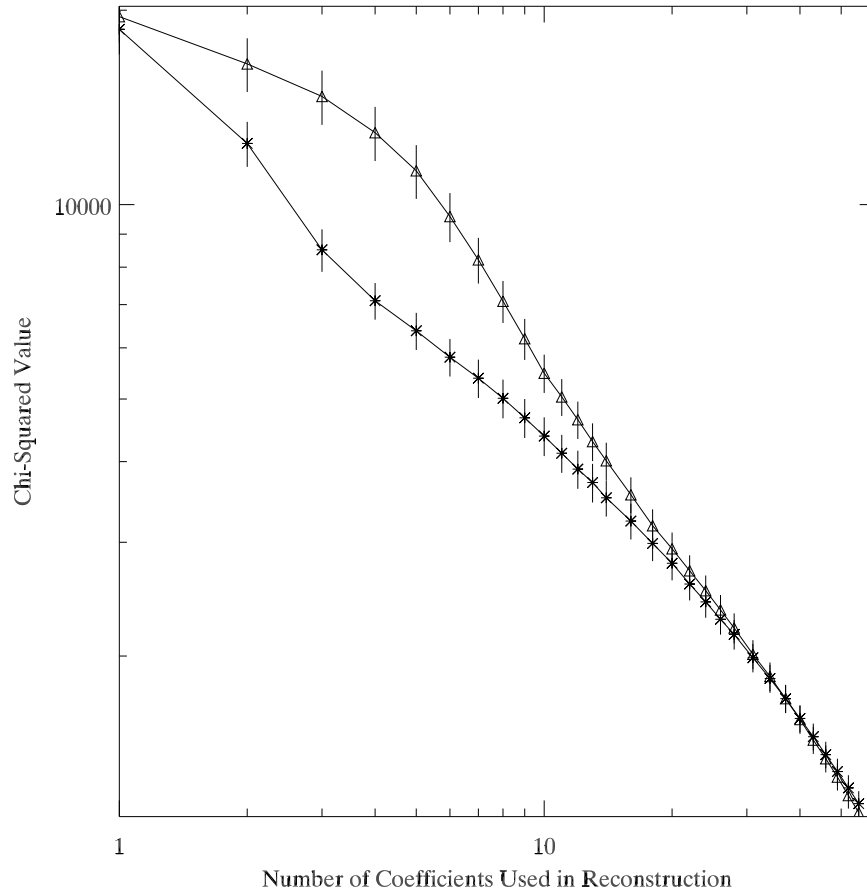


Fig. 13.— The mean chi-squared for all 196 Coma spectra for both the Daubeuchies4 (stars) and Symmlet8 (triangles) wavelets as a function of the number of wavelet coefficients used in the reconstruction of the spectra. The error is just the standard deviation observed between the Coma spectra. To avoid overcrowding, we have not plotted the similar curves for the Symmlet6 and Daubeuchies6 wavelets since they are worse than those presented here *i.e.*, they have a high χ^2 .

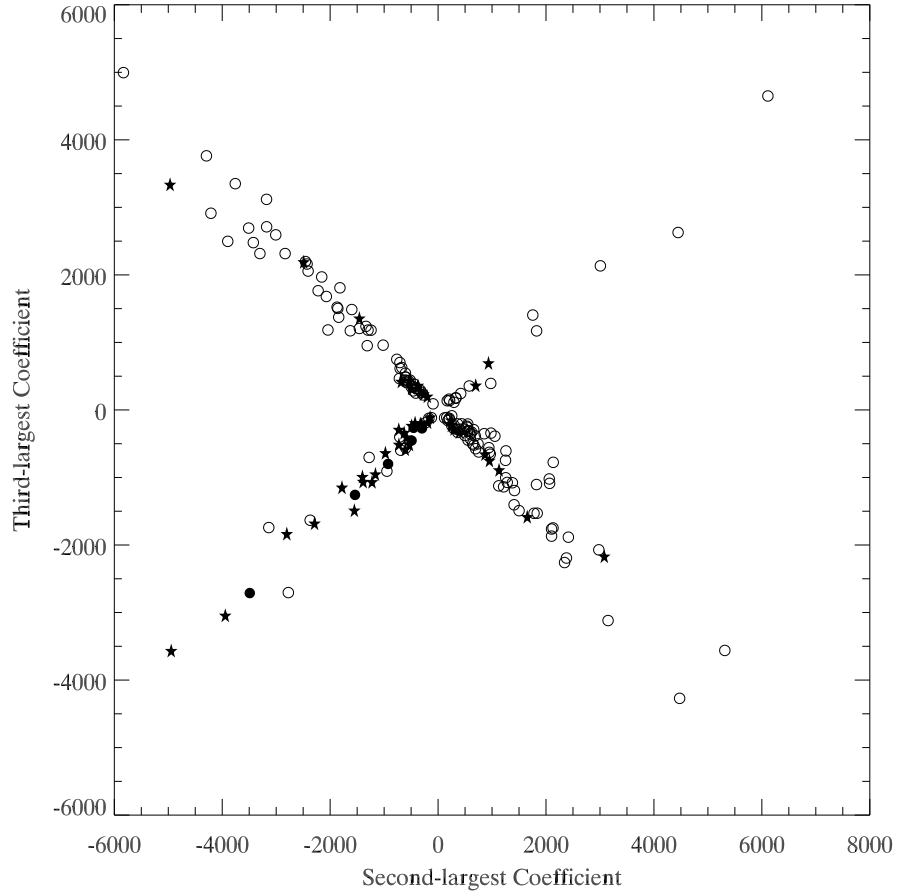


Fig. 14.— The second versus the third largest wavelet coefficient for all 196 Coma spectra. Open circles are absorption galaxies, solid triangles are emission line galaxies and solid circles are post-starburst (based on the initial visual classification). The “star-pattern” seen in the distribution of these points is simply the produced of our definition *i.e.*, the second coefficient must be larger (in absolute value) than the third coefficient.

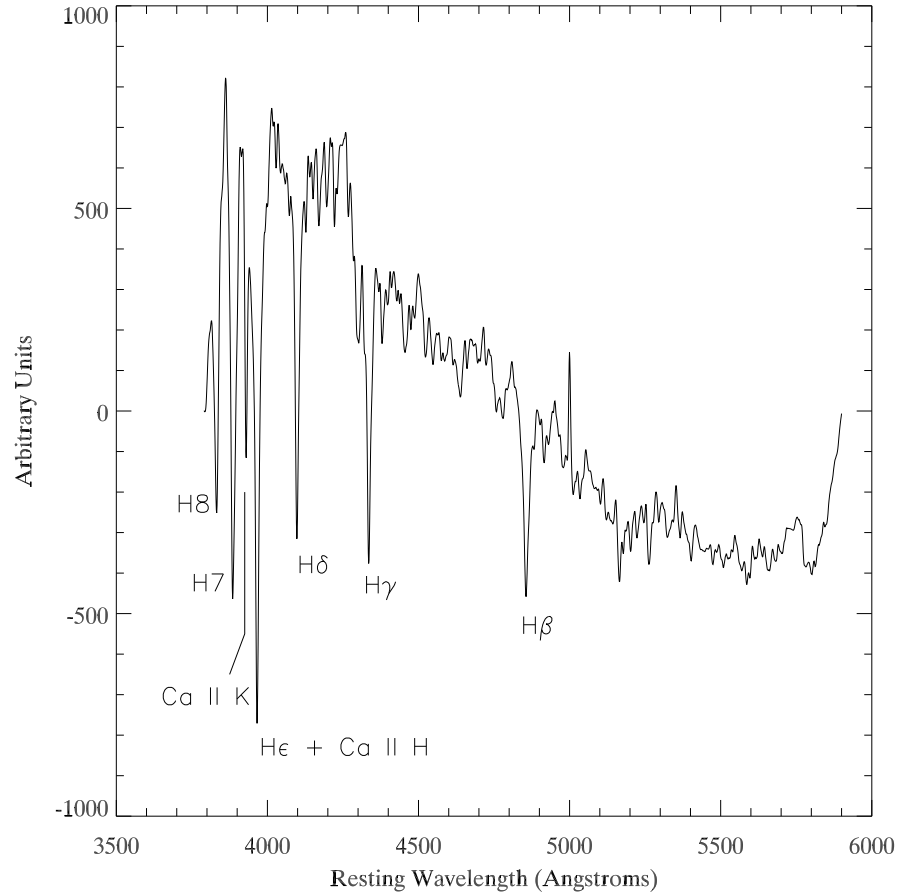


Fig. 15.— The co-added spectrum for 6 strong post-starburst galaxies visually identified in our SDSS Coma spectra. This plot illustrates the strong Balmer absorption features due to the young A stars. Also visible is the Calcium II H & K absorption features common in older galaxies. We have labeled the common absorption lines.

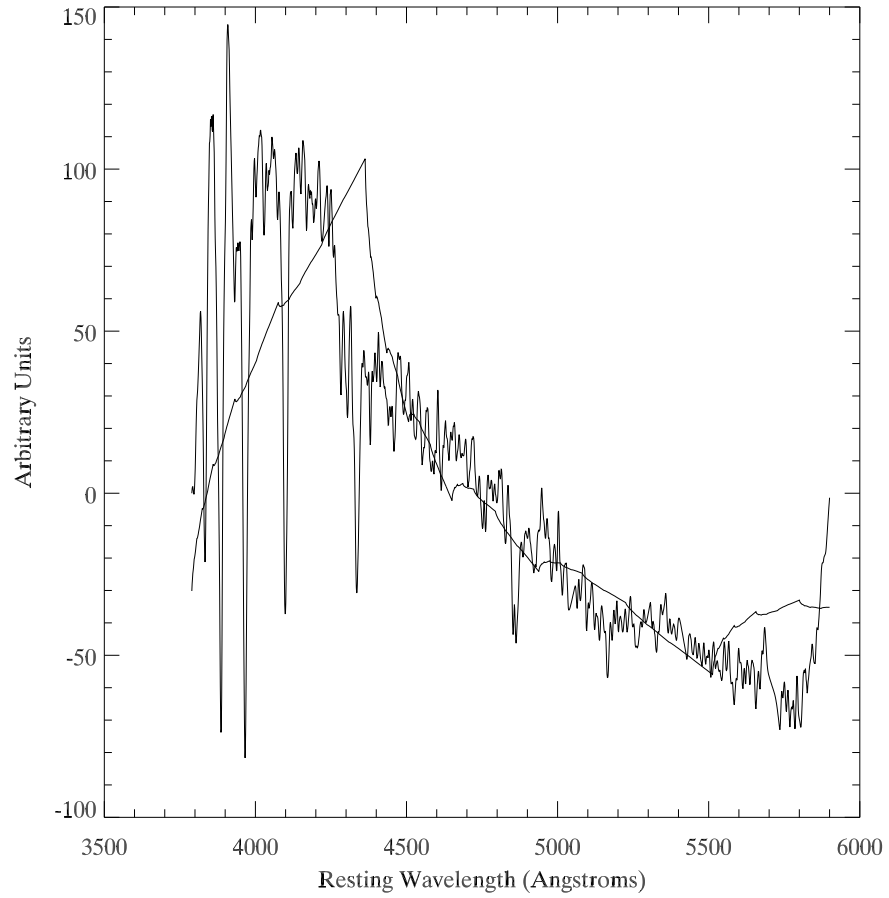


Fig. 16.— One of the strong post–starburst Coma galaxy spectra (same as presented in Figure 12) and the wavelet reconstruction based on just the three largest wavelet coefficients (see Figure 14).

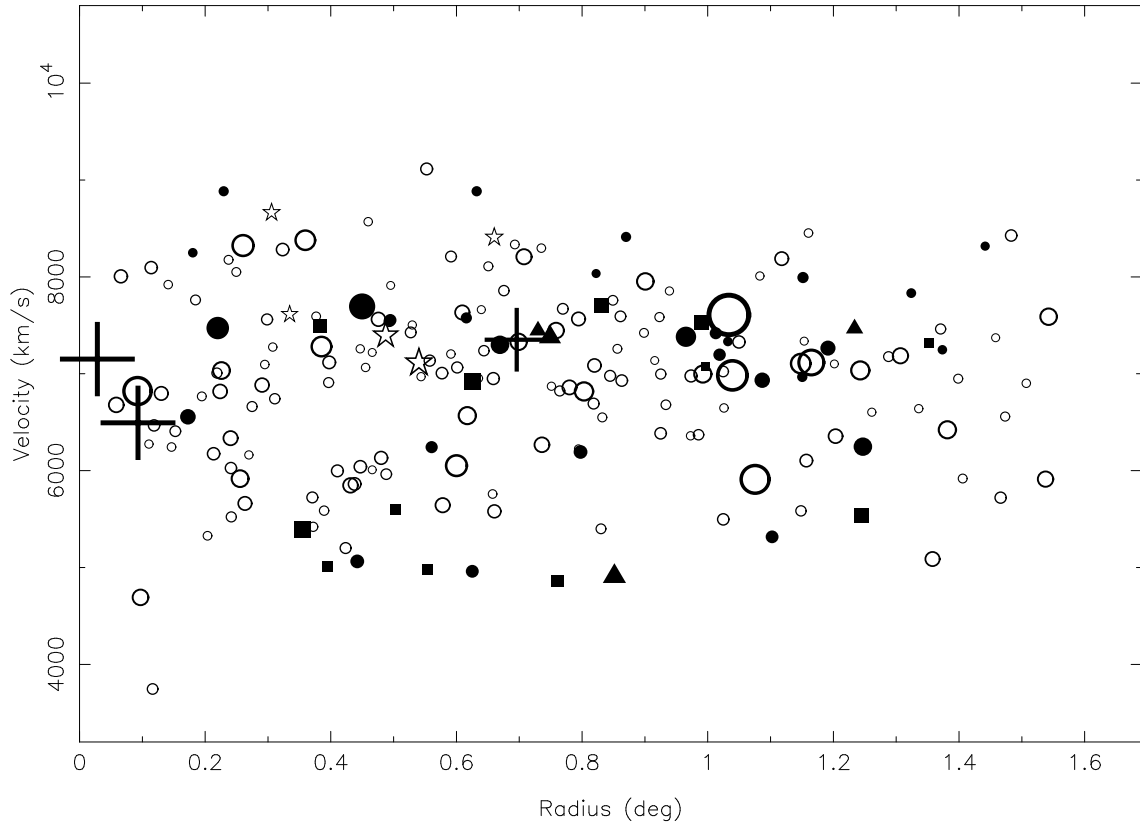


Fig. 17.— Distribution of radial velocities as a function of radius for the observed Coma galaxies. The symbols are the same as in Figure 3.

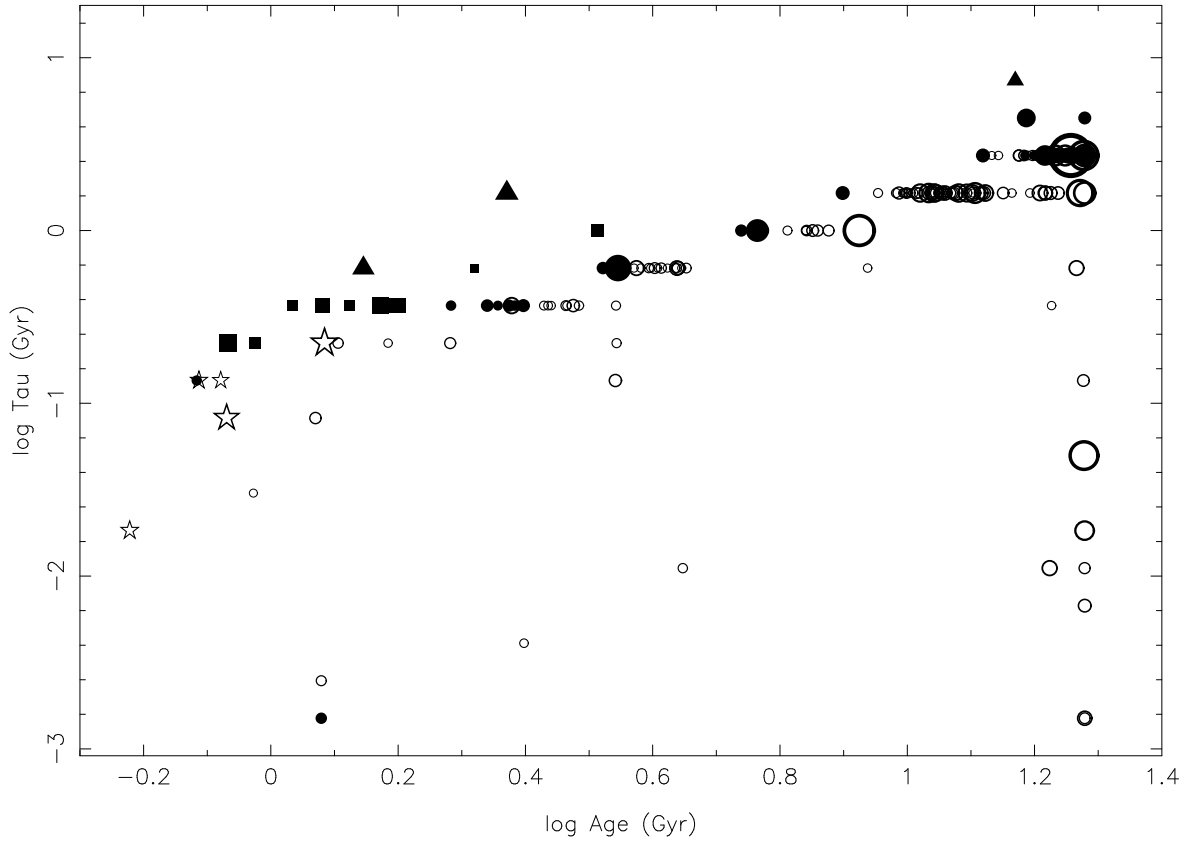
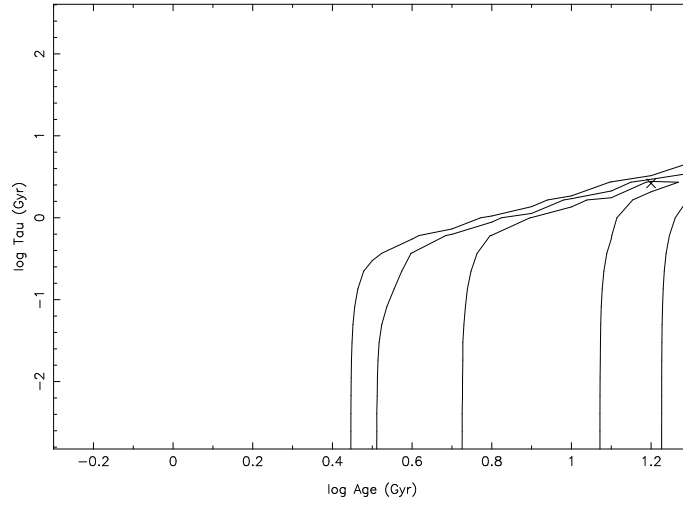
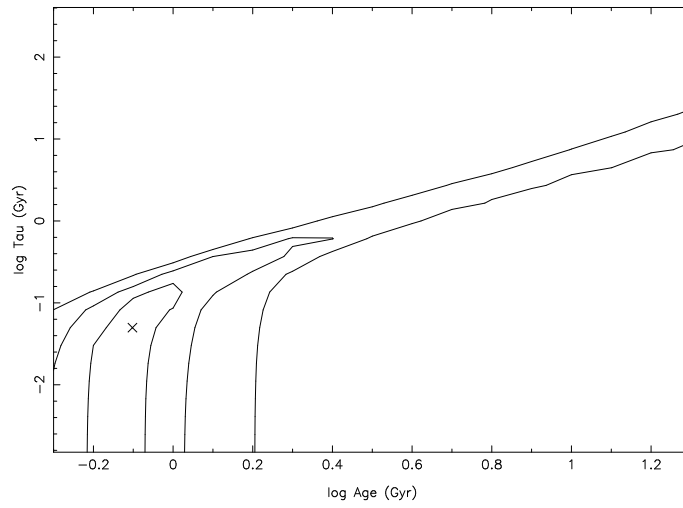


Fig. 18.— The star formation prescription versus age for all Coma galaxies (see text)

Fiber 143



Fiber 95



Fiber 117

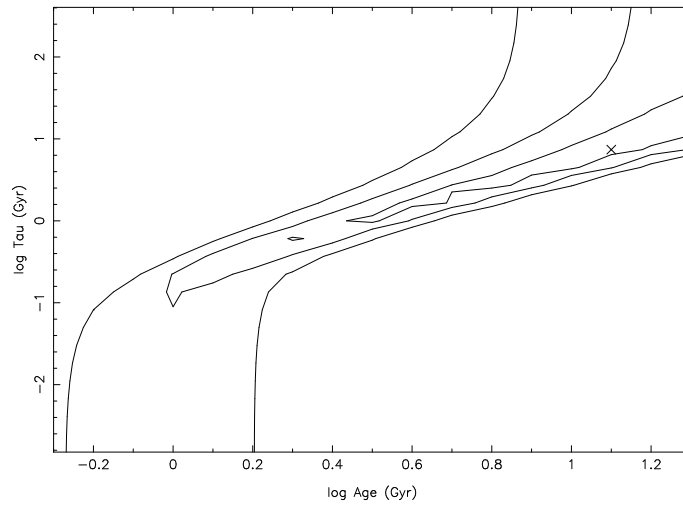


Fig. 19.— One, two and three sigma confidence levels contours for the spectral fit of three galaxies of different type. The cross signals the best fit age and τ parameter. Top: fiber 143 classified as **AB**; Middle: fiber 95, **PS**; Bottom: fiber 117, **EM+AB**.

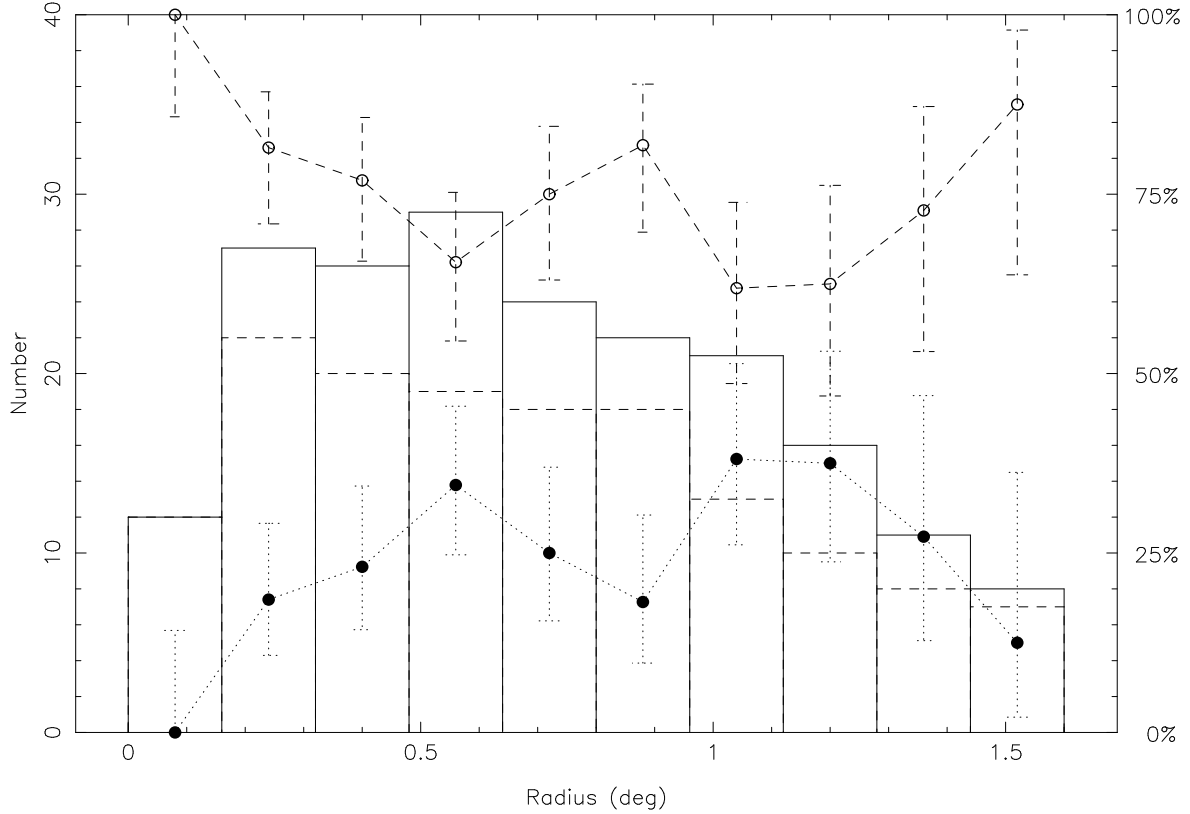


Fig. 20.— Number of observed Coma galaxies (solid histogram) and **AB** type galaxies (dashed histogram) as a function of projected radius. The left vertical axis provides the scale. The fraction of old stellar population galaxies (**AB**; open circles and dashed line) and active galaxies (**PS**, **AB+EM**, **EM+AB**, **EM**; solid circles and dotted line) are also plotted. The right vertical axis gives the scale. The errors in the percentages have been computed using the prescription of Gehrels (1986).